ABSTRACT

Manjari I. Rao

Analysis of a Locally Varying Intensity Template for Segmentation of Kidneys in CT Images

(Under the supervision of Edward L. Chaney, PhD)

The purpose of this study was to evaluate the use of a locally varying intensity template for automatic segmentation of kidneys in CT images. Kidney segmentation is often difficult because the surrounding soft tissue has varying contrast across the boundary.

A set of 60 CT images was selected for training. The images were manually segmented using a slice-by-slice contouring tool. Mean left and right kidney 3D medial models were computed along with corresponding Principal Geodesic Modes of variation from a population of models fit to this manual segmentation data. The models were referenced via an intrinsic coordinate system to obtain templates based on intensity profiles at different points across the boundary of the model. The resultant template-based segmentations were compared to Gaussian derivative template-based segmentations. There was marginal improvement in the quality of the segmentations and significant improvement in the degree of automation achieved using this method.

Acknowledgements

I would like to acknowledge Dr. Ed Chaney for his valuable guidance and encouragement, without whose support this work would not have been possible; Dr. Sarang Joshi and Dr. Carol Lucas, members of my committee, for their support; Dr. Steve Pizer, Joshua Stough, Gregg Tracton, for their willingness to help and patience in answering questions, and all the researchers comprising the Medical Image Display and Analysis Group.

Contents

List of Tables

List of figures

List of Abbreviations

CT	Computed Tomography
MRI	Magnetic Resonance Imaging
ROI	Region of Interest
M-rep	Medial Representation
3D/2D	Three Dimensional/Two Dimensional
PCA	Principal Component Analysis
PGA	Principal Geodesic Analysis

CHAPTER 1 - Introduction

The purpose of this thesis is to evaluate the use of a locally varying intensity template of the kidney for the purpose of automatic segmentation in CT images for radiation treatment planning. This chapter provides an introduction to radiation therapy and the procedures involved in treatment planning, primarily segmentation of anatomical structures.

1.1 Radiation Therapy and Treatment Planning

Cancerous tumors are made up of aggressive cells that have already beaten the immune system, allowing them to invade the surrounding tissue, or spread (metastasize) to other organs. *Radiation therapy* involves the delivery of a precisely controlled and monitored dose of radiation to a well-defined volume of tumor bearing tissue within a patient suffering from cancer. The radiation dose can be delivered by the use of radioactive implants, placed in the tumor region for a prescribed period of time, or by directing a beam of ionizing radiation, from an external source through the patient's skin towards the tumor region. The ionizing radiation deposits energy that destroys or injures cells in the area being treated, making it impossible for these cells to grow.

A key objective in radiation therapy is to uniformly irradiate the tumor, while minimizing the non-useful and potentially harmful radiation dose to other parts of the patient's body. The extent to which this can be accomplished depends on the location of the tumor and the characteristics of the radiation sources available. Tumors to be treated by radiation therapy may lie on the surface or at depths ranging from 1cm to about 15cm below the skin and their treatment may be complicated by the presence of radiosensitive organs such as eyes or spinal cord.

Modern methods of radiation treatment in oncology enable the precise destruction of tumor tissue and minimize side effects on the surrounding tissue by irradiating rays from different angles that intersect in the tumor area. An important consideration in the process of radiation therapy is the accuracy with which tumors can be localized and distinguished from the surrounding normal tissue.

The *radiation treatment planning* procedure that is performed prior to each treatment thus plays an important role in delivering high doses to the tumor while preventing the damage of critical normal structures, by defining the tumor volume with clinical examinations, operative findings, and from imaging studies such as *computerized tomography (CT), magnetic resonance imaging (MRI), radiography* with and without contrast media or other radiological examinations. Factors such as patient positioning, localization of tumor and vital organs, beam arrangement, appropriate dose, shielding and instructions for proper implementation of the treatment procedure should be taken into consideration for a good radiation therapy treatment plan.

1.2 Treatment planning for External Beam Radiotherapy

The process of external beam therapy planning can be divided into two stages:

- Simulation
- Treatment Planning

During simulation, the patient is placed in the treatment position on a special x-ray machine or CT scanner by the radiation therapist and simulation x-rays are taken. Masks, pads, or other devices may be used to help the patient to hold still during the simulation and treatment processes. The radiation oncologist then locates the tumor volume and the region to be treated on these images. The best arrangement of radiation beams needed to treat the patient are determined by the dosimetrist and the radiation oncologist, and then small marks are made on the patient by the radiation therapist to help guide the daily treatments.

For treatment planning, special computers and appropriate software are used to calculate the radiation dose that will be delivered to the patient's tumor and the surrounding normal tissue. The duration of time for which the treatment beam must be left on to deliver the prescribed dose is calculated.

Virtual simulation effectively integrates both simulation and treatment planning. It is a computer-aided design procedure in which 3D CT data information of a patient is used to build a computer-based graphical model of the patient for viewing tumor sites from different viewpoints, design the shape and angle of entry of irradiation

beams, and calculate dose distribution without the presence of the patient. After simulation and treatment planning have been completed, the treatment itself can begin.

1.3 Segmentation in Treatment Planning

In almost all radiation therapy centers in the US, radiation physicists and dosimetrists use *computer models* to plan the treatment. This computerized treatment planning allows the treatment to be delivered more accurately. Images of the patient are acquired before treatment from a CT or MRI scanner. The first step in the treatment planning process is the identification and *contouring* or *segmentation* of all targets and normal structures on each CT/MRI slice.

The process of segmentation can be defined as splitting an image into segments that hold some property distinct from their neighbor. It is the basic requirement for the identification and classification of structures in an image. Segmentation is a process of extraction of information from an image in such a way that the output image contains much less information than the original one, but the little information that it contains is much more relevant to the purpose of the task. Such a classification can be approached from two points of view; by identifying the edges that run through an image or by identifying regions within an image.

Segmentation of medical image data is one of the most difficult tasks in image processing, and on this point the human visual system is still considered superior to

the computer. The procedure in clinical settings is performed using techniques similar to drawing programs. Typical planning systems depict both tumors and sensitive normal tissues in 3-dimensional space for every patient. Manual segmentation is quite tedious, though still the fundamental means of planning in most radiation treatment cases. However, manual outlining also has its limitations. The segmentation result is dependent on the operator's experience and may also change for every trial by the same operator. It is also often difficult to identify structures on a two-dimensional CT image, especially when the normal anatomy has been altered by the presence of an infiltrating tumor. Objects of interest in the human body are non-rigid structures which change continuously day-to-day. The complexity is increased when one considers alternate planes of orientation, i.e., coronal or sagittal.

Application of automatic segmentation techniques to medical images for radiation treatment planning can save time and reduce inter and intra-operator variability. The present automatic segmentation methodology investigated in this study is based on the intensity variation perpendicular to the boundary of a given structure to be segmented, the kidney in this particular study. The idea is to apply an intensity template based on statistics generated on a population of images which would stabilize the method and provide good agreement with human performance.

CHAPTER 2 - Background

The first part of this chapter briefly discusses a particular class of *medial models*, called m-reps, as an effective means of representation and segmentation of anatomical objects. The second part focuses on the challenges in the segmentation of kidneys in CT images.

2.1 Shape representation via M-reps

The automated approach used in the present study is based on representing anatomical structures in 3D using the concept of *medial models* [Blum 1962, 1967, 1973], known as “M-reps” [Pizer 1999 and Joshi 2001]. M-reps are medially based solid models that are particularly effective in representing anatomic objects in 3D and capturing geometric information in deformable model based segmentation approaches.

By definition, a medial axis is a locus of the centers of spheres that are bitangent to the boundary of the object being represented (Fig.2.1). The center point of each such sphere is a point on the medial surface, and the radius of each sphere defines the radius function at that point on the medial surface. While the medial axis is a curve for objects in 2D, it is represented by a sheet for objects in 3D. Thus, the

surface of an object in 3D can be recreated given all the points on the medial locus and the associated radius. This is the basic idea behind shape representation using medial models.

(a) (b) (c) (d)

Fig.2.1. A 2D figure represented by (a) boundary (b) bitangent circles in the figure (c) medial axis (d) protrusion represented by a branch in the medial axis

The present study focuses on the use of single-figure m-rep models for segmentation, i.e., the simplest m-rep consisting of a single figure with a non-branching medial locus. An m-rep model consists of a grid of medial 'atoms', each of which is made of a hub and a pair of spokes. While the hub is the center of the relevant bitangent sphere inside the object, the spokes are the radii to the points of tangency (Fig.2.2).

Each medial atom of an m-rep contains information regarding the coordinates of the medial sheet at a sample point ***x***, the distance from ***x*** to the object boundary or

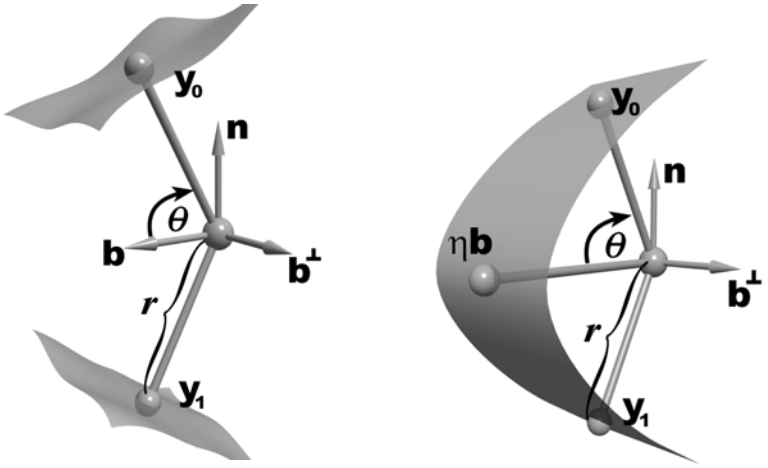

Fig.2.2. (a) Figure illustrating a Medial atom (b) Boundary implied by an end atom. (See Pizer et al, IJCV 2001 for complete discussion)

radius *r*, the two vectors of length *r,* representing the spokes which point to the points of tangency of the inscribed sphere, the angle *Θ* formed between each of the spokes and the angular bisector vector ***b***, and a frame F = (**n**,**b**,$\mathbf{b}^{\perp}$) that defines the tangent plane of the medial sheet at ***x***. Another parameter *η*, elongation, is defined by atoms which lie on the outer edges of a mesh and specifies the curvature of the object about that point (Fig.2.2).

M-rep models are represented by an object based coordinate system defined by (u,v,t,τ) (Fig.2.3), where *u* and *v* represent the row and column corresponding to the position of the medial atom, $t \in$ [-1,1] indicates which side of the locus the point lies on, i.e., *t* = -1 or +1 for internal medial points and runs continuously around the crest region from –1 through 0 at the boundary through +1, and τ measures the distance along the spokes from the boundary with $\tau > 0$ outside the boundary, $\tau < 0$ inside the boundary and τ = -1 at the medial locus. This object-intrinsic coordinate system

provides spatial and orientational correspondence between an m-rep in two different states of deformation.

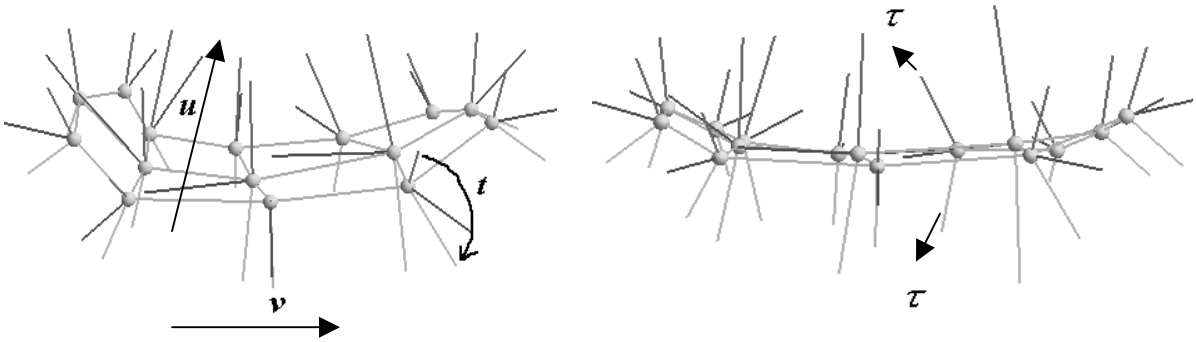

Fig.2.3. M-rep coordinate system represented by (u,v,t,τ). The figures illustrate the variation of these coordinates along the medial axis.

The medial locus is sparsely sampled to produce an approximate surface of the m-rep or the 'implied boundary' (Fig.2.4). The real surface lies somewhere within a collar region, discussed in Section 2.2.

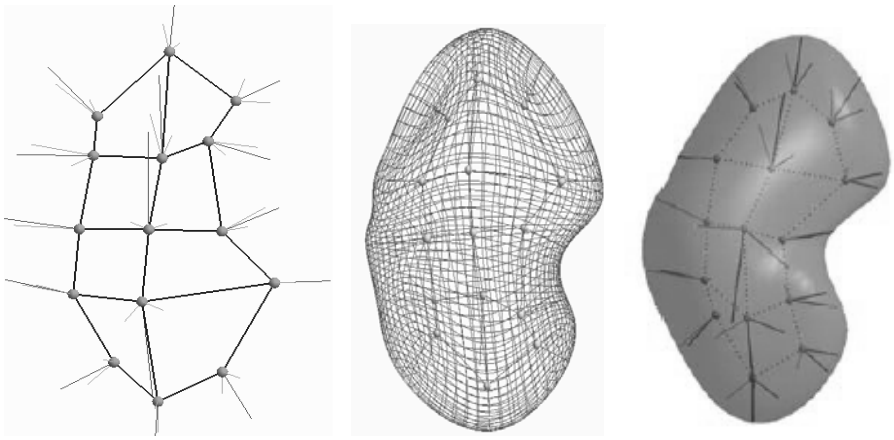

(a) (b) (c)

Fig.2.4. (a) Example of a mesh of medial atoms for a kidney (b) Wire frame surface rendering of the boundary implied by the medial mesh (c) 3D surface rendering of the boundary implied by the medial mesh.

2.2 Segmentation using M-reps

One of the main advantages of m-reps is that they allow classification of object deformations into along-object deviations, namely elongations and bendings, and across-object deviations, namely bulgings and attachment of protrusions or indentations (multifigure m-reps). An additional advantage is that distances can be expressed as a fraction of medial width. These properties allow positions and orientations to be followed through deformations of elongation, widening, or bending [Pizer et al, IJCV 2001].

Overview

The m-rep segmentation process can be briefly described as follows:

The method operates from large to small-scale levels, at each level *deforming* the m-rep model by optimizing in a Bayesian framework, an objective function over a set of geometric transformations available at that scale level. The *objective function* is the sum of two terms, namely, a term that measures the geometric typicality of the deformed m-rep (comparison of corresponding points in an m-rep before and after deformation) and the geometry to image match term (comparison of intensities at corresponding positions).

M-rep segmentation begins with interactive initialization to position the kidney model near the target kidney in the image data. Fully automatic segmentation proceeds through several stages at successively smaller levels of scale:

1) Transformation of the whole kidney model based on both the similarity transform and Principal Geodesic Analysis or PGA that optimize the objective function based on the model and the image data; this involves translation, rotation, scaling of the entire model according to the similarity transform and shape variation based on the Principal Eigen modes of a mean model.
2) Deformation of each medial atom in the model, in turn and recursively until convergence of the objective function is achieved. This involves translation, rotation and scaling of each individual atom of the medial mesh.
3) Fine-scale surface refinement, i.e., each surface tile of the implied surface is shifted along its normal to optimize the objective function. This scale was not used in the present study.

The transform that is performed on the m-rep model in the first step is based on the fact that medial descriptions are elements of a Lie group and uses Principal Geodesic Analysis or PGA to define the shape variability of the object. PGA is a statistical means of describing shape variability similar to Principal Component Analysis or PCA in Euclidian vector space [Styner 2001]. PCA is only applicable when model parameters are elements of a Euclidian space and medial parameters are not naturally elements of a Euclidian space. But they have been shown to be

elements of a Lie group [Fletcher et al 2003] and so the variations in shape can be statistically defined by the principal components of a geodesic mean (Fig.2.5) generated from a population of medial models.

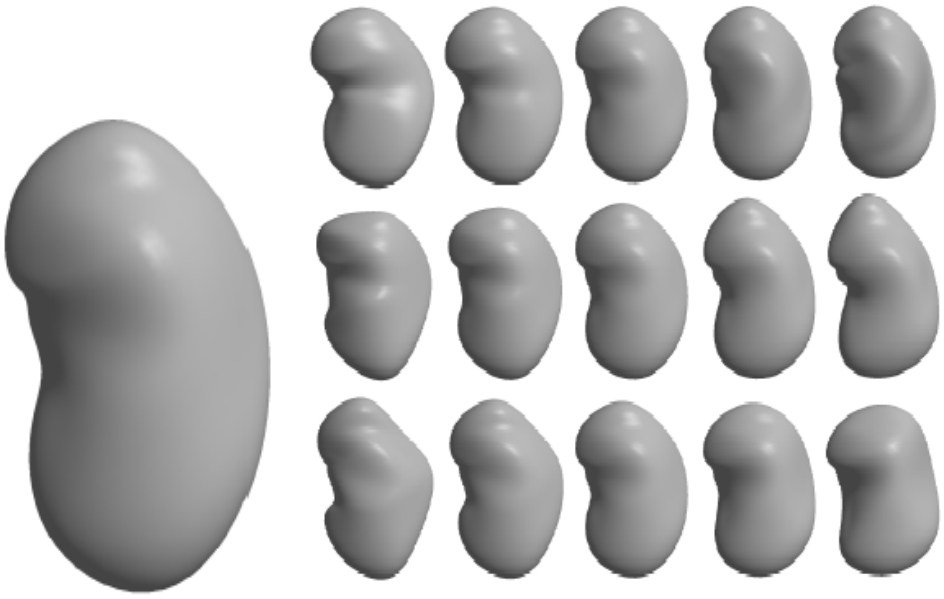

(a) (b)

Fig.2.5. (a) The mean kidney model (b) The first three principal modes of deformation of the kidney m-rep. Each row displays the models corresponding to $\{-3\sqrt{\lambda_i}, -1.5\sqrt{\lambda_i}, 0, +1.5\sqrt{\lambda_i}, +3\sqrt{\lambda_i}\}$, along the i^{th} principal component.

Deformation of individual atoms in the next step, involves establishing a geometric correspondence between the deformed model and the initial model by measuring the displacement of each individual medial atom from its initial position in the m-rep as well as its relationship to the image data and its' neighboring atoms. The neighborhood of a medial atom is made up of its immediately adjacent atoms.

An atom of an m-rep after deformation, identified by its figural coordinates illustrated in Fig.2.3, can be compared to the corresponding atom before deformation and the magnitude of the *r*-proportional distance between these points can be used to measure the local deformation (Fig.2.6). Calculating *geometric typicality* is done in terms of relating an atom's coordinates predicted by the stage immediately previous to the current deformation stage, and by its neighbors at the current stage which enforces a local shape consistency with the model.

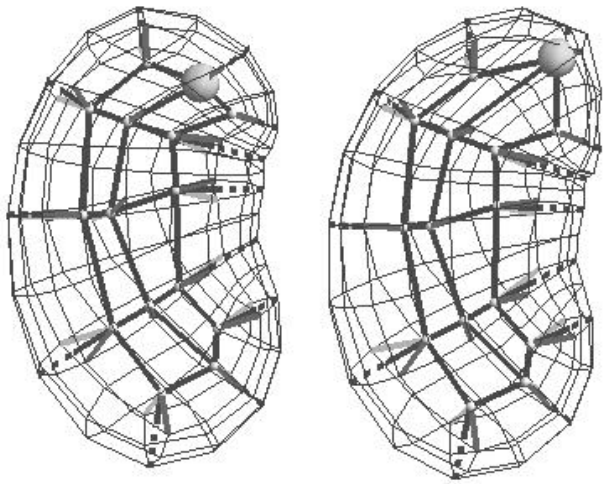

(a) (b)

Fig.2.6. 3D medial mesh of a kidney m-rep. (a) Initial model (b) Deformed model with change in position shown by the highlighted atom.

The *match* between geometry and the image is based on a model template. A 'template' defines a target pattern at different locations in an image and gives maximum response when the intensity values of the pixels in the image correlate to the values at the same locations specified by the template. In the m-rep segmentation approach, it can be considered as a filter indicative of the presence of

a boundary of an object. This template is determined by training the model on a data set with known truth, which is taken to be user-approved segmentations. The template is defined only in a mask region defined by the set of figural coordinates discussed in Section 2.1. The width of the mask is choosable as a collar symmetrically placed about the boundary (Fig.2.7), with a width that is proportional to the object width at every point on the boundary. It is chosen by subdividing the boundary positions with a fixed mesh of m-rep figural coordinates (u,v) (Fig.2.3) and then choosing spatial positions to be spaced along each medial spoke (implied boundary normal) at that (u,v). These along-spoke positions are equally spaced in the figural distance coordinate up to a plus or minus a fixed cutoff value.

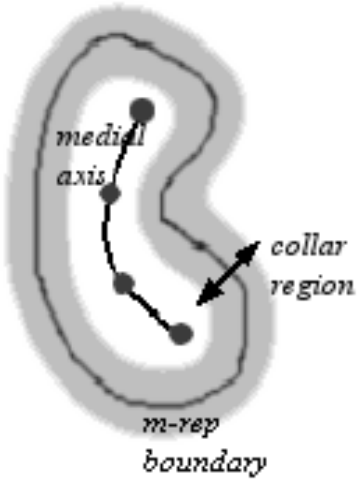

Fig.2.7. The collar region for a kidney m-rep forming the mask for measuring geometry to image match in 2D

For the present study, this cutoff value was 0.3, i.e., from -0.3r to 0.3r with 0 at the boundary. This corresponds to a boundary-centered Gaussian in the collar region,

$$G(x) = \frac{1}{\sqrt{2\pi}\sigma} e^{-\frac{x^2}{2\sigma^2}}$$

with a standard deviation half the width of the collar, i.e., σ = 0.15 for the present study.

2.3 Kidney Segmentation

Automatic extraction of kidneys from CT images is very challenging under typical conditions for treatment planning even with excellent image quality and initialization parameters. The crowded soft tissue environment that surrounds the kidney makes it hard to distinguish it from structures such as the adrenal gland, since the organs have similar consistency and are often pushed against each other. Most soft tissue also does not contrast strongly against its background.

This particular study focuses on the kidney primarily because the kidney is an organ which is at high risk due to radiation exposure during treatment of abdominal and pelvic tumors. For this reason, the kidney is one of the primary organs that is segmented during radiation treatment planning to ensure that it does not receive an unacceptably high dose of radiation.

Another reason for choosing the kidney as the organ of interest for this study is that the kidney is a fairly simple organ, which has a well-defined shape in most cases. The automatic segmentation methodology, which uses m-reps for shape

representation, is in the developmental stage and the kidney is an excellent example to study initially since it can be represented by a single figure object. It is located in a fairly distinguishable position in the body and is also identifiable by surrounding structures such as the liver, spleen and spinal cord.

The present study addresses the fact that different parts of the kidney boundary have different types of surrounding structure and thus a single intensity description of the whole boundary is insufficient to achieve a good segmentation. For example, right kidneys have completely different intensity variations along the boundary adjacent to the liver (Fig.2.8). The goal of the study is to investigate a method for characterizing intensity variations at points on the surface of the kidney by three canonical profiles that are discussed in detail in Chapter 3.

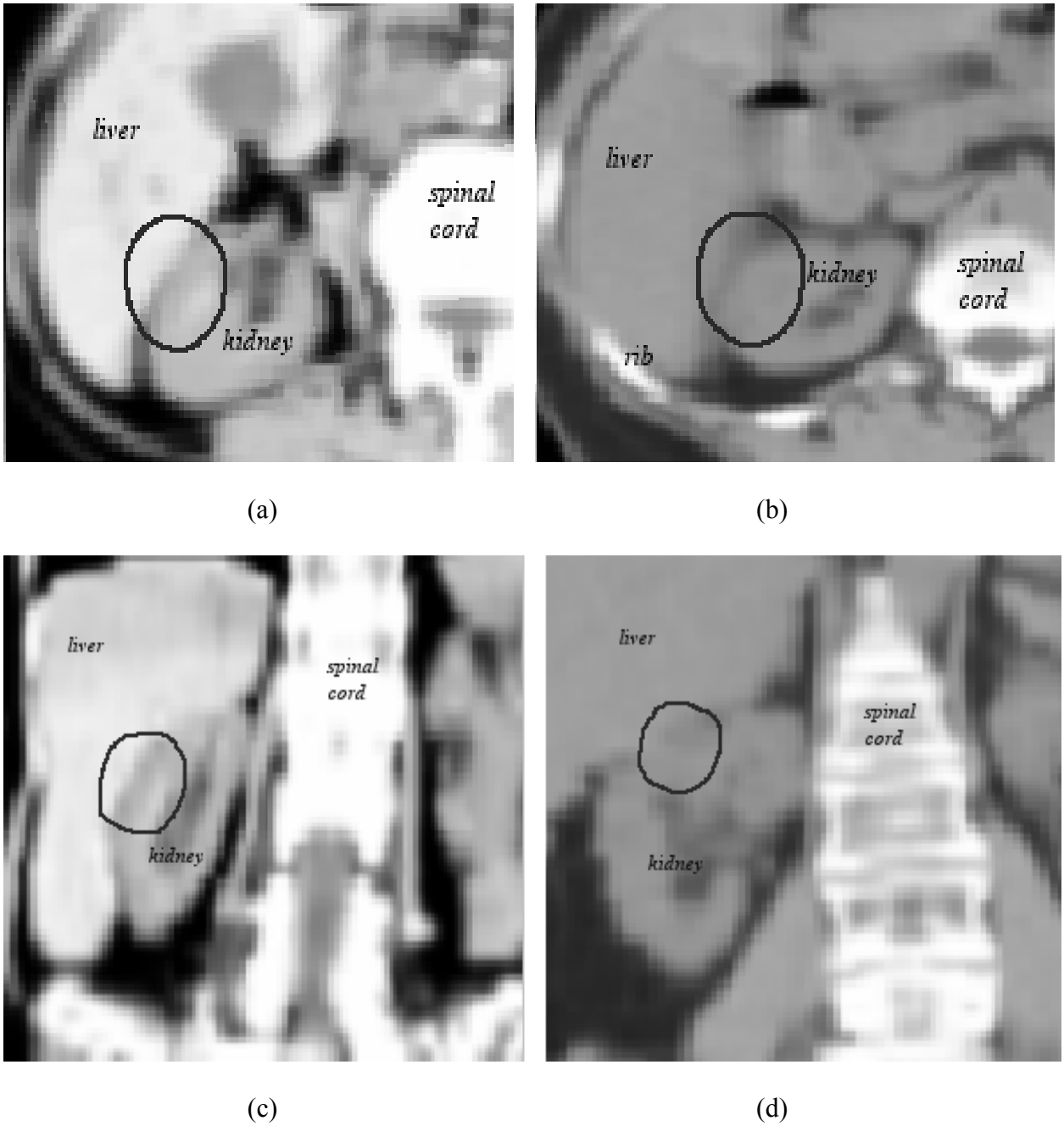

Fig.2.8. A particular region along the boundary of the right kidney in two images.

(a) Axial view- region where kidney is adjacent to the liver and liver appears brighter
(b) Axial view- similar region, but kidney and liver have same intensity values
(c) Coronal view- same region as (a) above, where the liver appears brighter
(d) Coronal view- same region as (b) above

CHAPTER 3 – Materials and Methods

The first part of this chapter provides information about the CT images that were collected for this study based on a set of selection criteria for training and target purposes. Training involved generation of a medial model from a population of kidneys as defined by CT images and a corresponding locally varying intensity template. The next section focuses on the implementation of the method on the target image set using the locally varying intensity template.

3.1 Template Match

The image match for segmentation with m-reps in previous studies, was measured using the directional derivatives of a Gaussian defined in the entire collar region as described in Chapter 2 (Section 2.2). This made use of a single profile at each point on the surface of the m-rep (profiles are elaborated in Section 3.3 of this chapter). The locally varying intensity template used in the present study can be defined as an intensity template which is a function of figural positions along the boundary of an m-rep, obtained from a set of training images that can be used for correlation in the target image to produce a geometry to image match measurement.

3.2 Training and Target Images

The study required a set of training images to create the kidney m-rep and a set of target images to evaluate m-rep segmentation. The kidney m-rep was created by analyzing a population of training kidneys starting from their boundaries. The training set was also used to obtain intensity profiles that in turn were used to generate the template for the kidney m-rep. The target images were a set of 12 images (24 kidneys in all), on which the study was conducted. Most of the images had a raster resolution (number of pixels per slice) of 512 X 512. The pixel size ranged from 0.098mm X 0.098mm to 0.156 X 0.156 for the images.

All the images used for this study were CT images obtained from the Department of Radiation Oncology, University of North Carolina at Chapel Hill. The scans were collected using a Siemens Somatom Plus 4 CT scanner. A database of over 700 images was screened to select training images suitable for this study. The data included scans of various sections of the body, from head and brain structures, lungs to the pelvis and feet. Not all the images that kidneys present could be used for the study. Each of the images had to pass certain criteria for final selection. The images had to be carefully chosen since they constituted the training set of kidney data which had to encompass both the complete kidney geometry as well as surrounding intensity information for both kidneys.

Table 3.1 on the following pages summarizes the criteria involved in the selection of training images.

Table.3.1. Criteria for selection of training CT images.

Criteria	*Comments*
1. Presence of whole kidney(s).	The CT scans had to completely include either or both kidneys. Diseased or abnormal kidneys were rejected.
2. Position of patient during scan (Fig. 3.1).	Images obtained for the purpose of radiation treatment usually involve the patient lying supine, i.e., on his/her back with head towards the gantry and feet away from it, unless otherwise necessary. Since the training method used a statistically generated intensity template for the kidney, the position of the kidney with respect to surrounding organs had to be consistent in the images.
3. Absence of contrast agent.	Presence of a contrast agent or 'dye' in a patient alters intensity values in an image, by enhancing contrast (Fig.3.2).
4. Absence of tumor, disease or kidney stones.	Tumors, disease and kidney stones also alter intensity values in an image (e.g., stones in the kidney are deposits of calcium which have a different intensity when imaged as compared to a healthy kidney).

Table.3.1. Criteria for selection of training CT images

5. No more than moderate motion artifacts.	Motion artifacts in CT images (Fig.3.3) are produced if the object is not static, e.g., due to respiration or cardiac pulsation.
6. Margin of at least 2cm on the superior and inferior edges of the kidney.	To provide sufficient surrounding intensity information for training and segmentation.
7. Slice thickness less than or equal to 5mm per slice.	Thinner slices provide better spatial resolution and structural detail.

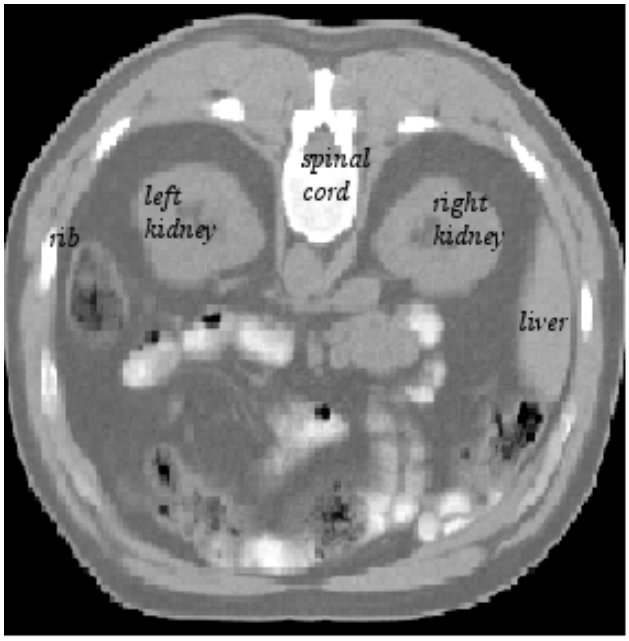

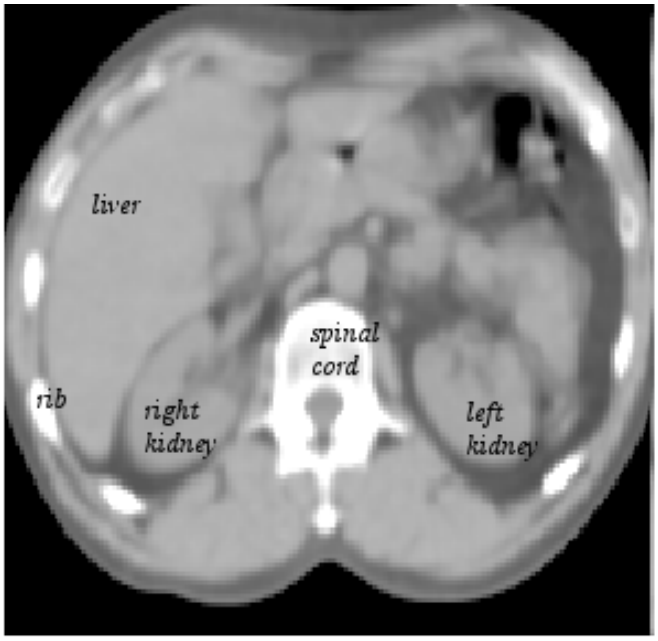

Fig.3.1.1. Patient in prone position Fig.3.1.2. Patient in supine position

Notice the variation in the position and hence the variation in intensities of the kidney relative to surrounding structures between the two images

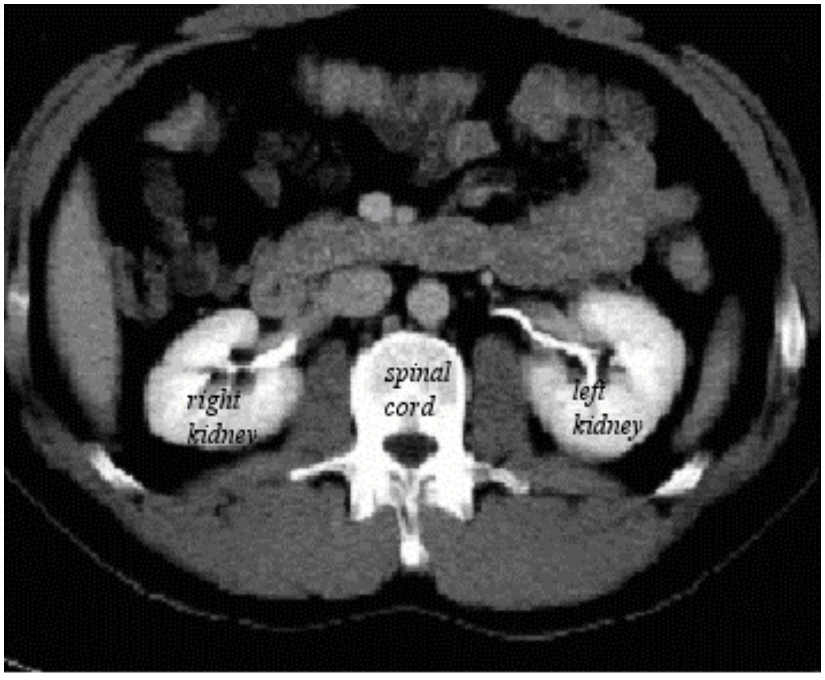

Fig.3.2. CT image with contrast. Notice that the intensity of the kidney is brighter as compared to the surrounding structures.

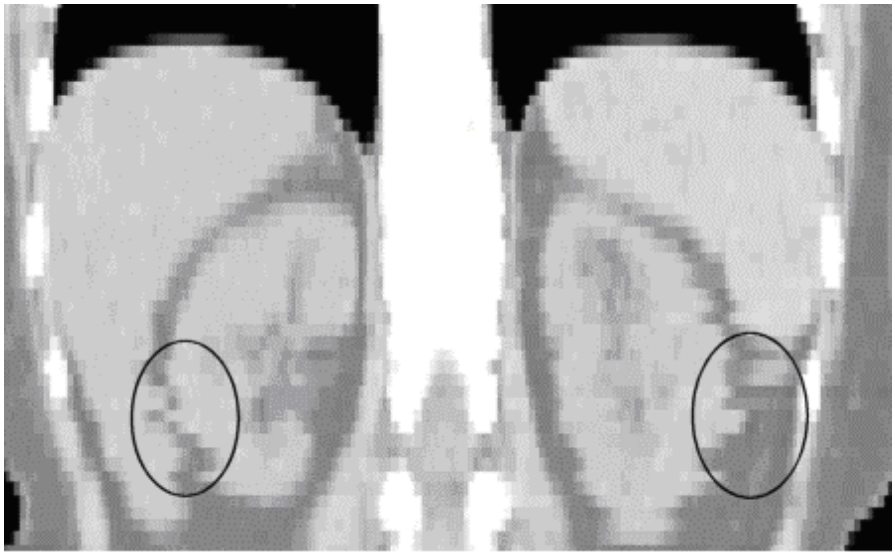

Fig.3.3. CT image of the kidneys with strong motion artifacts due to breathing. ROI is indicated.

Method

3.3 Generation of a Locally Varying Kidney Template

The process of generating the intensity profiles for the kidney to statistically produce a single 'template' involved the following steps:

1. Hand segmentation of kidneys from the training set (Fig.3.4).
2. Conversion of the contours into a blurred binary image (Fig.3.5).
3. Deformation of an m-rep model into the blurred binary images produced in step 2 (Fig.3.6), to produce a mean model with principal geometric modes of variation via PGA.

4. Generation of intensity profiles at many points on the surface of the segmented kidneys (Fig.3.9 and Fig.3.10) by correspondence with the respective training gray-scale images.
5. Classification of each of the intensity profiles from step 4 into one of three categories, based on the best match among three analytic filter types (Fig.3.11).

The final step in the study was the segmentation of kidneys in the target images using the locally varying intensity template to compute image match (Fig.3.15 through Fig.3.20).

Manual segmentation of the training images was performed using software similar to drawing tools for painting and tracing. The contours were traced on each 'axial' or cross-sectional slice using the mouse and cursor. Intensity windowing was carried out to enhance the contrast of the displayed image during segmentation.

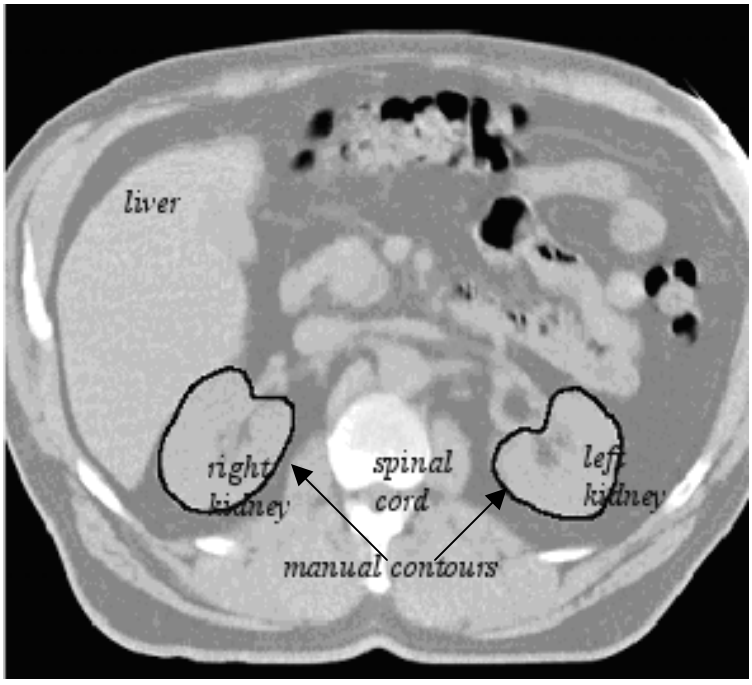

Fig.3.4. Cross-section (Axial) slice-by-slice contours

(Software: *Anastruct_editor* - part of the PLanUNC suite of RadioTherapy Tools, developed at UNC Radiation Oncology since 1986 by George Sherouse, Edward Chaney, Tim Cullip, Gregg Tracton, Julian Rosenman and others.)

The output of the hand segmentations was a series of cross-sectional contours which represented the kidney for each individual training image. These 'contour stacks' were used to generate binary images, i.e., images that have only two intensity values (0 for black and 1 for white). A Gaussian smoothing operator was applied to these images to produce smooth edges (Fig.3.5). The standard deviation of the Gaussian operator varied for each image and was the equivalent of one cubic voxel of each image (approximately 1mm - cubic voxel sizes in the training images ranged from 0.98mm to 1.5mm).

(a) (b)

Fig.3.5. (a) Binary image of the kidney created from a stack of manual contours
(b) Smoothed image created by applying a Gaussian operator to (a)

The m-rep kidney model used in the study was generated using the population of the hand segmented training kidneys, by defining shape variability using *Principal Geodesic Analysis* (PGA) described in Chapter 2. A single figure medial mesh of 15 atoms (3 columns and 5 rows) was fit into each of the training binary images (Fig.3.6) via the automatic segmentation method described in Chapter 2, to generate an m-rep segmentation for each kidney in the training data set [Dam 2003]. The fit of the m-rep model to the training binary images was achieved using the Gaussian

derivative template for the image match since the boundary of the kidney in these images could clearly be defined by the Gaussian derivative. The mean model and the principal modes of variation corresponding to that mean were calculated from this population of kidney m-reps [Fletcher 2003]. The initial m-rep model was replaced by this mean and the process of fitting the kidney m-rep into the training binary images was iterated until the mean converged to an m-rep model that did not vary much from the previous iteration. This mean kidney m-rep was used for further training to generate the locally varying intensity template.

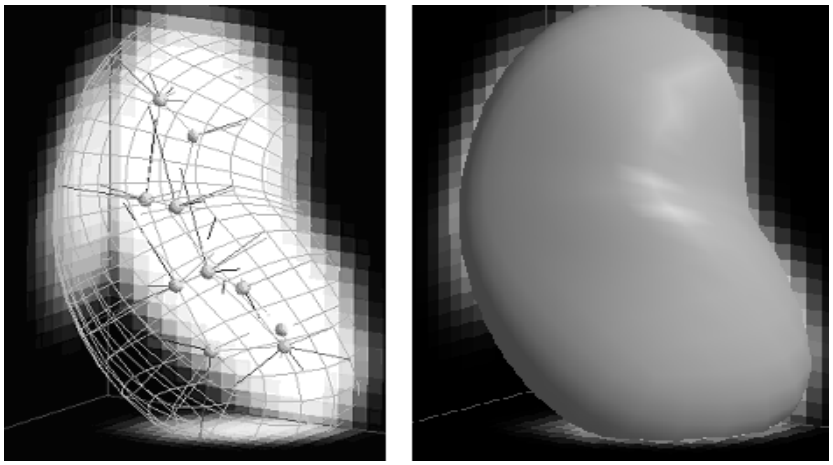

(a) (b)

Fig.3.6. (a) M-rep model of a kidney in 3D fit into a training binary image – the boundary is represented by a wire frame (b) Boundary represented by a solid surface

For generating the intensity template for this study, three analytic filters were considered (Fig.3.7), light-to-dark (higher intensities in the kidney as compared to surrounding structures), dark-to-light (lower intensities in the kidney as compared to

surrounding structures) and a 'notch' (similar intensities in the kidney as well as surrounding structures with a narrow dark region in between).

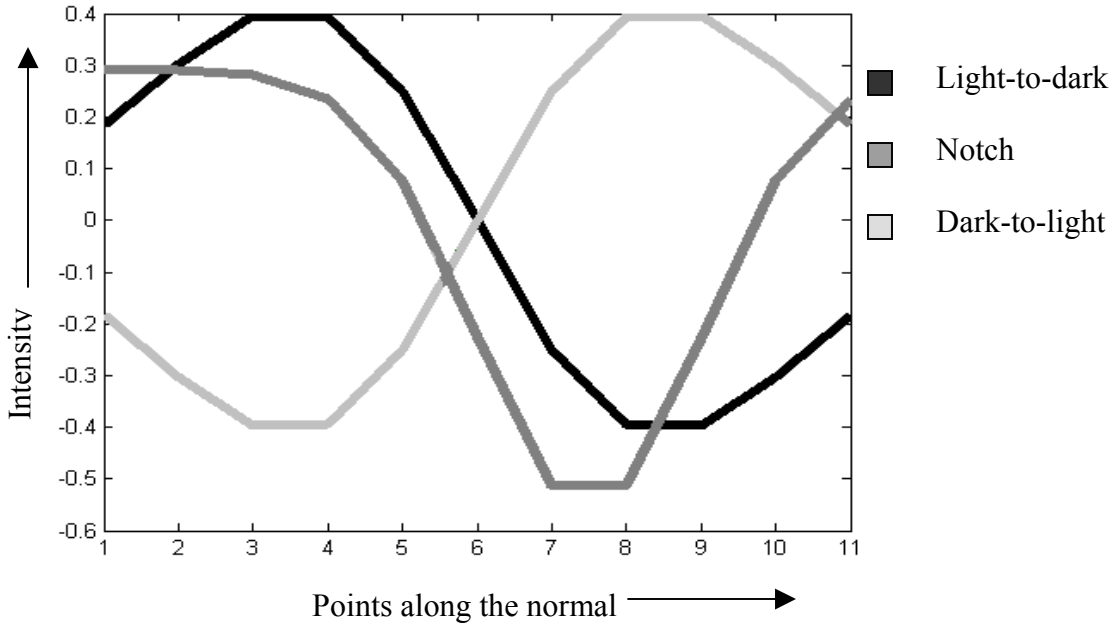

Fig.3.7.Initial Analytic Filters

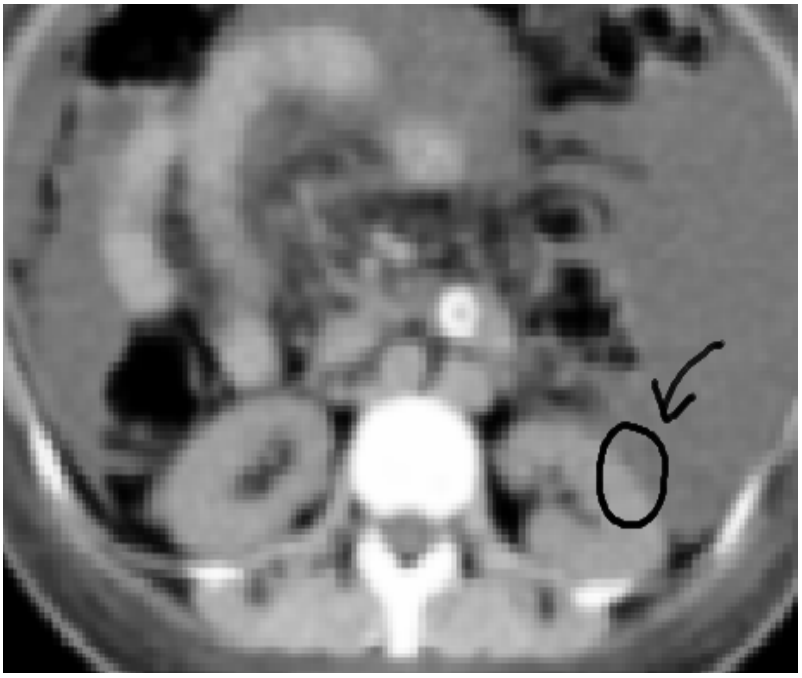

(a) Image region corresponding to the light-to-dark filter (ROI is marked)

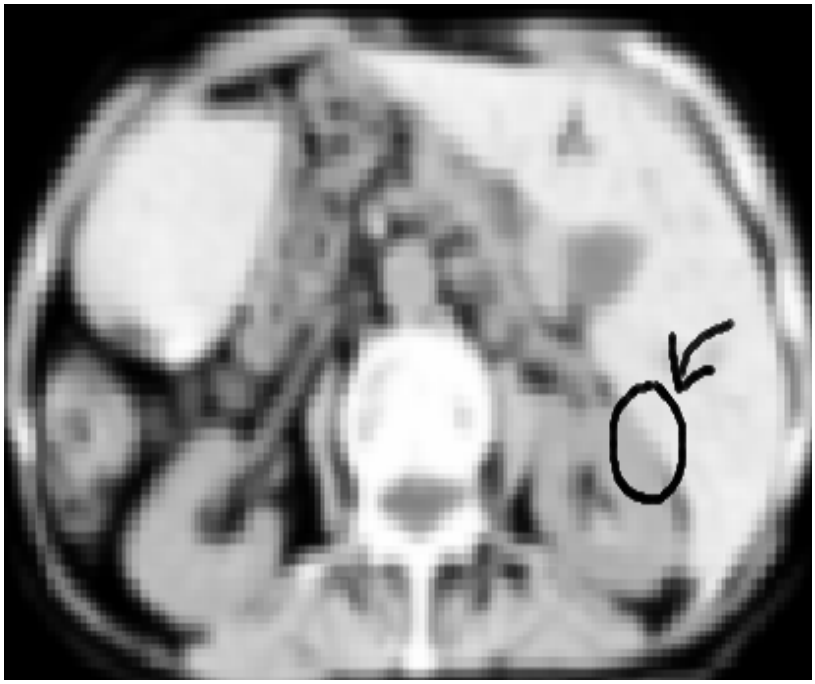

(b) Image region corresponding to the dark-to-light filter (ROI is marked)

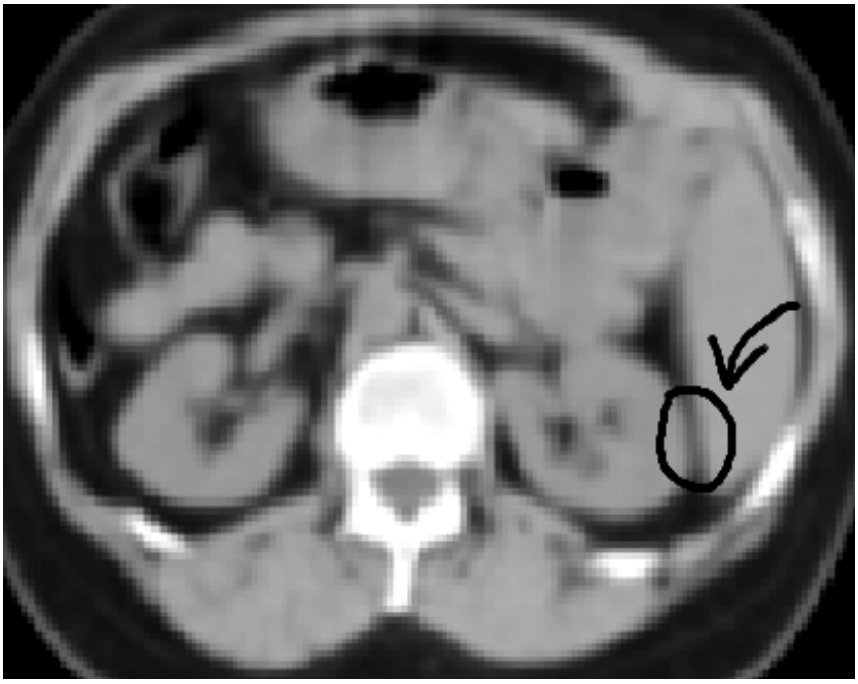

(c) Image region corresponding to the notch filter (ROI is marked)

Fig.3.8.Images corresponding to the three filters above. The regions of interest are indicated.

The end points of the spokes of the outer atoms in the medial lattice of an m-rep are linked together to form a quadrangular mesh surface. This surface is subdivided by applying a variant of subdivision surface methods [Catmull 1978] described by [Thall 2002], which provided a natural framework for defining the boundary at 2562 (Fig.3.9) points on the surface of the m-rep. At each point, a normal of length 0.*6r* (*r* being the length of the spoke of a medial atom, and the normal going from –0.3*r* inside the m-rep to 0 at the boundary and 0.3*r* outside, defined by the collar region described in Chapter 2) was generated.

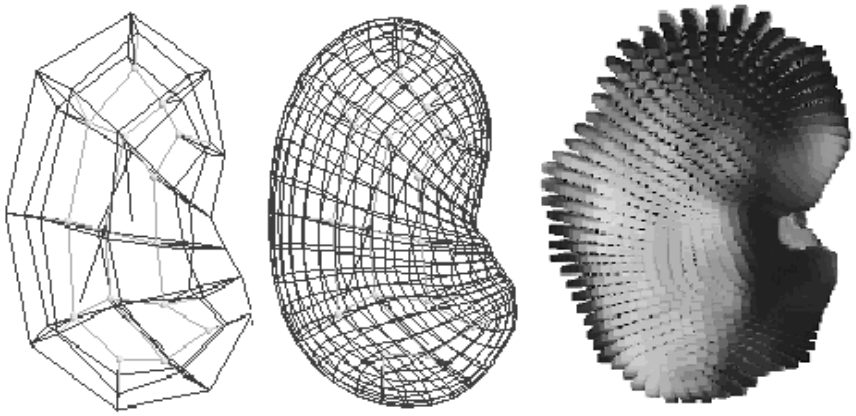

(a) (b) (c)

Fig.3.9. Surface of the kidney m-rep formed by (a) linking the ends of the spokes of edge atoms (b) subdividing the quad mesh in (a) by interpolation (c) 3D rendering of the kidney m-rep defined by 2562 points on the surface

Each normal was sampled at 11 different points (Fig.3.10) to generate an intensity profile at each of the 2562 points along the surface of the m-rep. The sampling rate was chosen as 11 based on the resolution of the training images, to be able to capture sufficient intensity information since the collar region (0.6*r*) was approximately 11 pixels in width for these images.

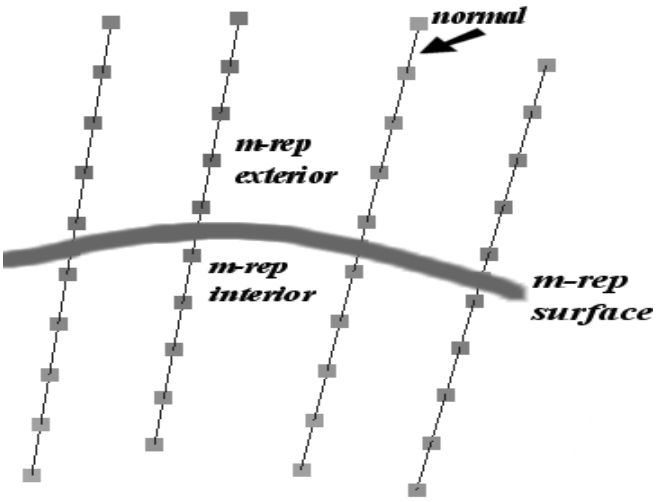

Fig.3.10. Normals drawn at points on the surface of the m-rep sampled at 11 points with the 6^{th} sample being the point on the surface of the m-rep

The mean m-rep kidney model was used to segment each of the blurred binary images from the training data set and the normals at the 2562 points on the surface of each training m-rep were similarly sampled. The intensity values corresponding to each of these points along the normals were obtained from the corresponding points in the training gray-scale images. These intensities defined the *profiles* at all the 2562 points on the surface of the m-rep.

The above process resulted in a large number of intensity profiles (2562 times the number of training cases for each kidney). To determine the intensity template, the three analytic filters shown in Fig.3.7, were applied to the profiles collected at each point. The responses were computed by taking the dot product of the profiles with each of the filters. In other words, if **X** is considered as the vector defining a profile at a particular boundary point and **Y** is the vector defining one of the analytic filters then,

$$\mathbf{X} \cdot \mathbf{Y} = \sum_{i=1}^{n} x_i y_i = x_1 y_1 + \ldots + x_n y_n$$

is defined as the response at that particular point to the filter. The highest response among the three filters for each point determined the filter type classification for that point (Fig.3.11).

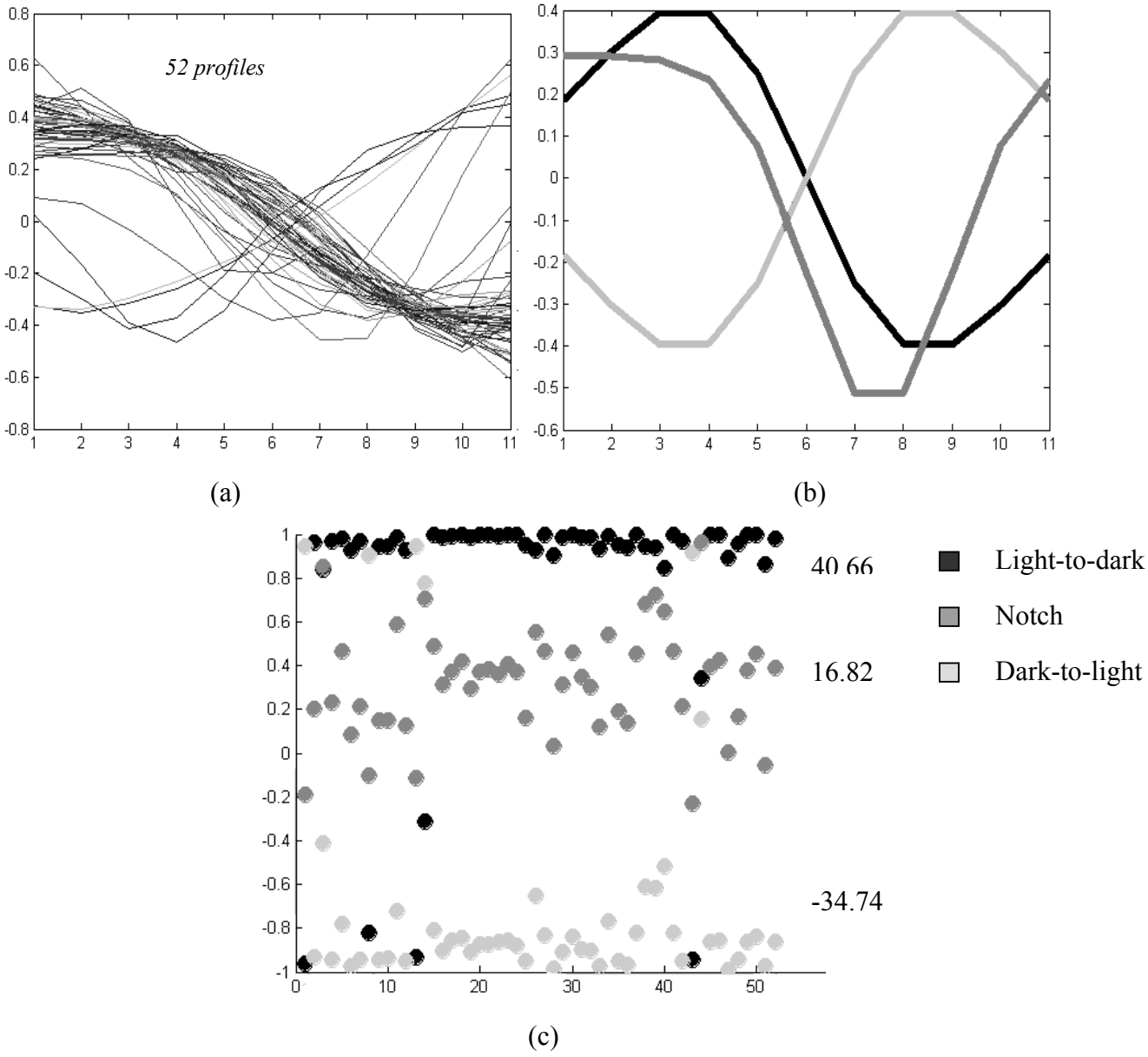

Fig.3.11. Example illustrating the response of a profile drawn at the same point on the surface of an m-rep for all 52 right kidneys. (a) Intensities at 11 different points along the

normal at a particular point across 52 training right kidney m-reps (b) Initial Analytic Filters (c) Responses of each of the profiles for all 52 cases obtained by taking the dot product of the profile with each of the three filters. The sum of all the responses for each filter is indicated on the right of the plot. For this particular point, the sum of responses for the light-to-dark filter, 40.66, was the highest.

Each profile collected from the training images was placed in a bin corresponding to the analytic filter giving the best response to the dot product. The means of the profiles in each bin were calculated and the three initial analytic filters were replaced by these mean filters. The entire procedure was repeated until the mean profiles converged to a stable shape (Fig.3.12). These converged filters were used for the final intensity templates.

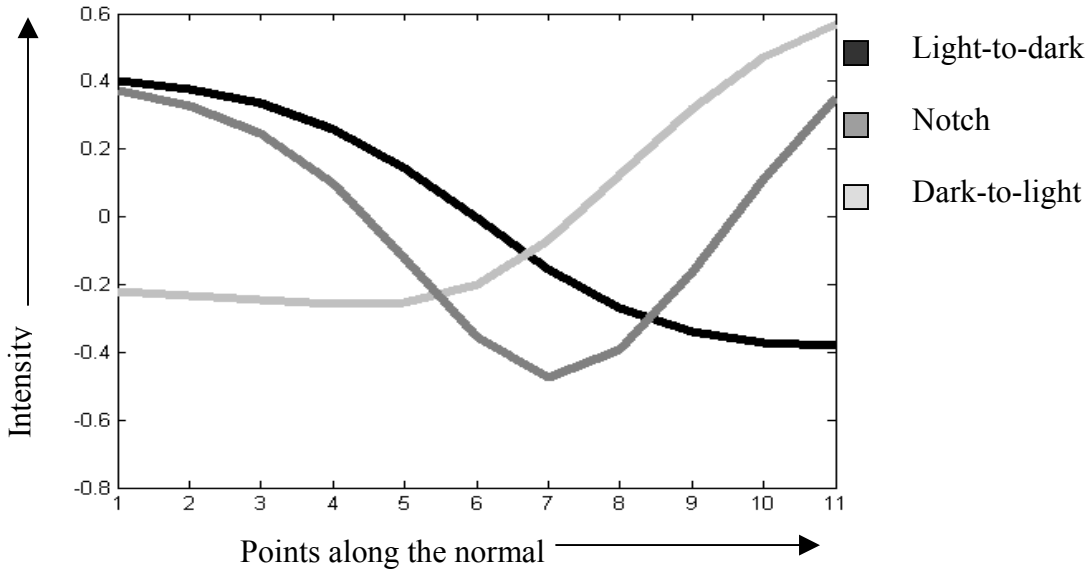

Fig.3.12. Converged Mean Filters

To determine which filter to assign to each of the boundary points, the responses (Fig.3.11) to each of the three converged mean filters for all 2562 points over all the

training cases were calculated in same procedure as stated before. These responses were then summed and the filter which had the highest value over all the cases was decided as the filter to be used at that particular point along the surface of the m-rep (Fig.3.11). The same procedure was repeated for all the remaining points for both the left and right kidneys which resulted in the filter distributions shown in Fig.3.13 and Fig.3.14.

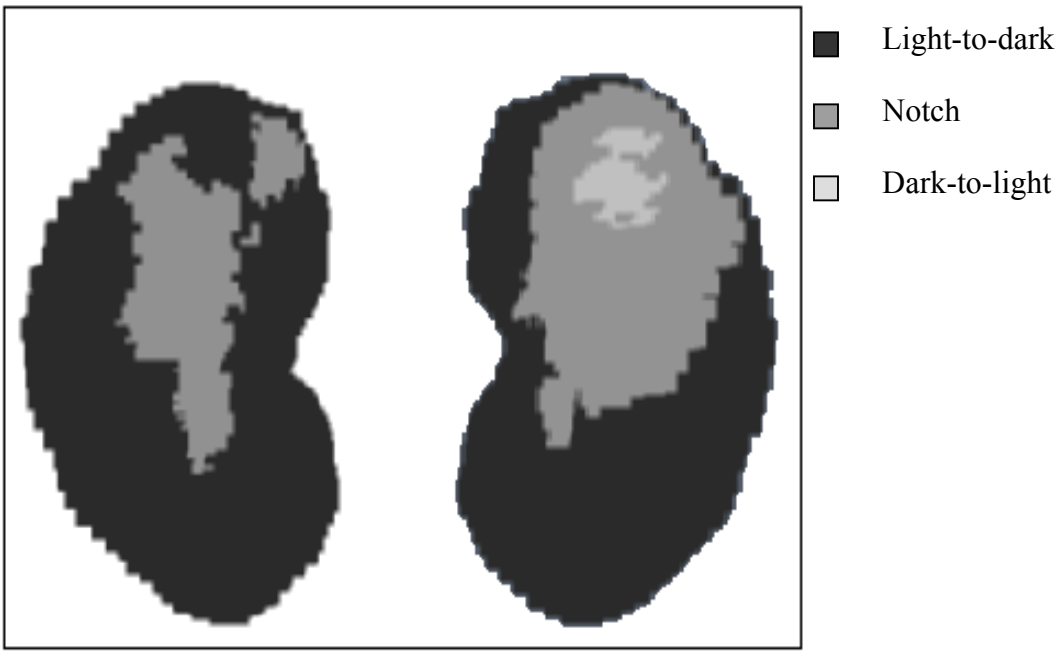

Fig.3.13. Distribution of the three mean filters over the surface on both sides of the Right Kidney

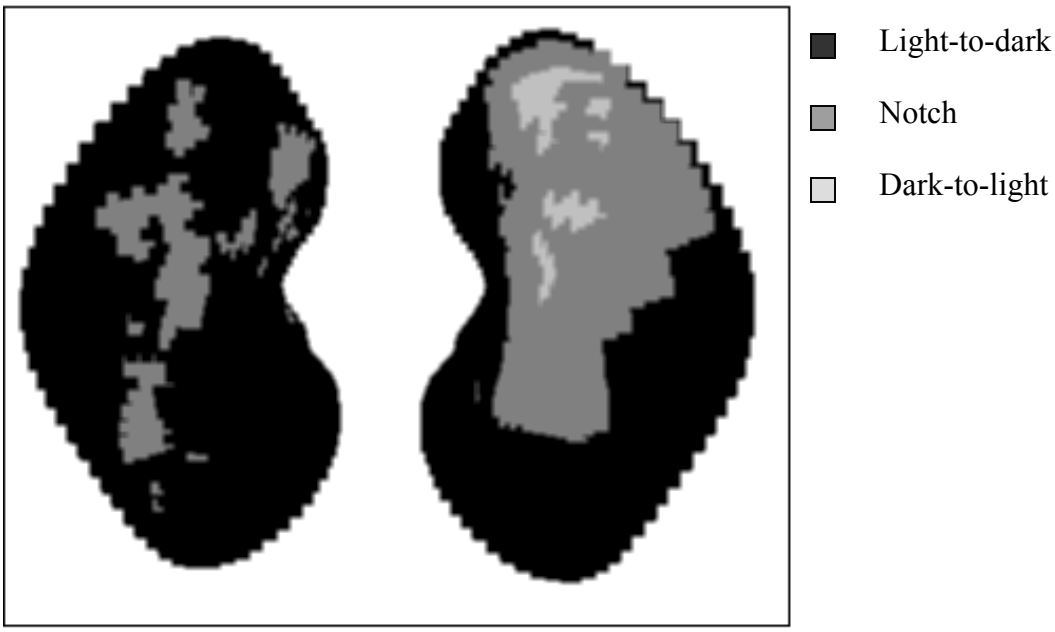

Fig.3.14. Distribution of the three mean filters over the surface on both sides of the Left Kidney

3.4 Segmentation of Target Images

The intensity template generated as described in Section 3.3 was used to segment kidneys in target CT images (Fig.3.21 and 3.22) via the m-rep deformation method described in Chapter 2.

The following figures illustrate typical segmentations for six cases from the target image data set. The initial hand placements (black contours) and final segmentations (white contours) are shown.

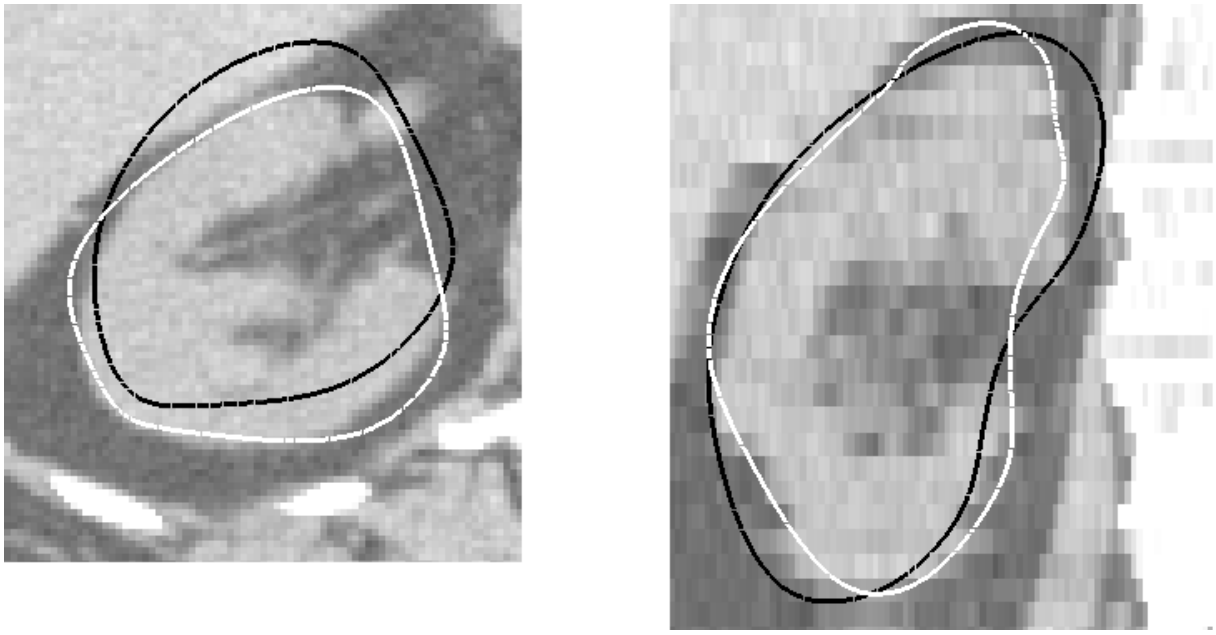

(a) (b)

Fig.3.15. Case 646R, Right Kidney - Initial Hand Placement (black contour), Final Segmentation (white contour) - (a) Axial View (b) Coronal View.

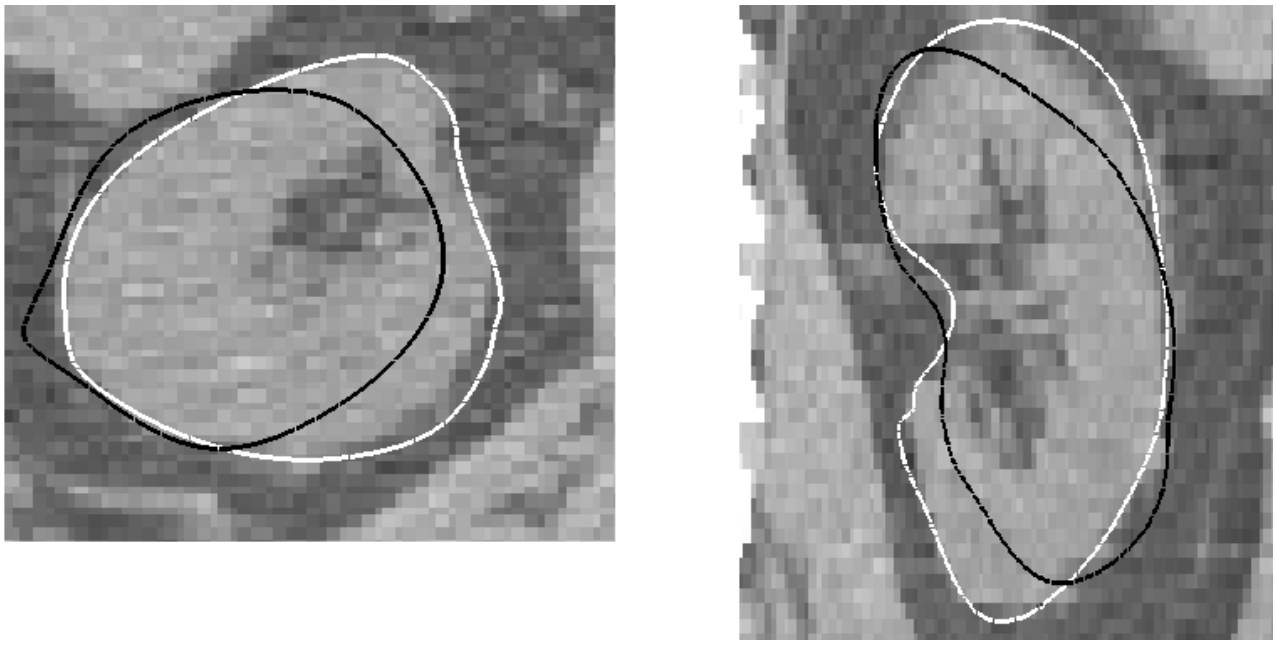

(a) (b)

Fig.3.16. Case639L, Left Kidney - Initial Hand Placement (black contour), Final Segmentation (white contour) - (a) Axial Slice (b) Coronal Slice

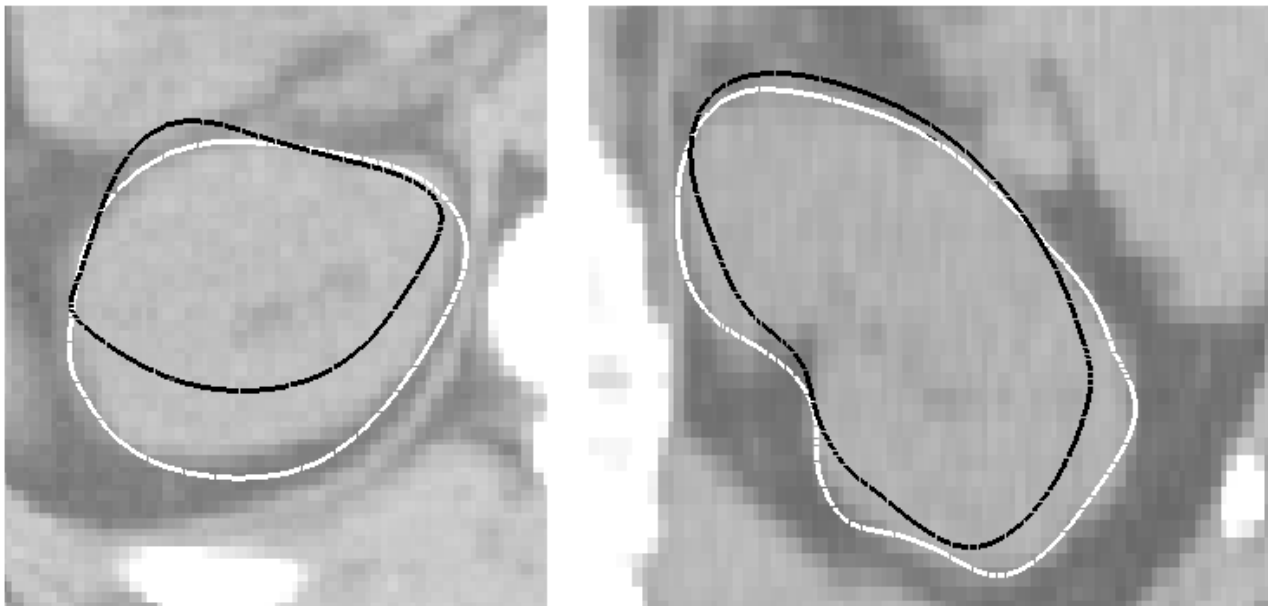

(a) (b)

Fig.3.17. Case 648L, Left Kidney - Initial Hand Placement (black contour), Final Segmentation (white contour) - (a) Axial Slice (b) Coronal Slice

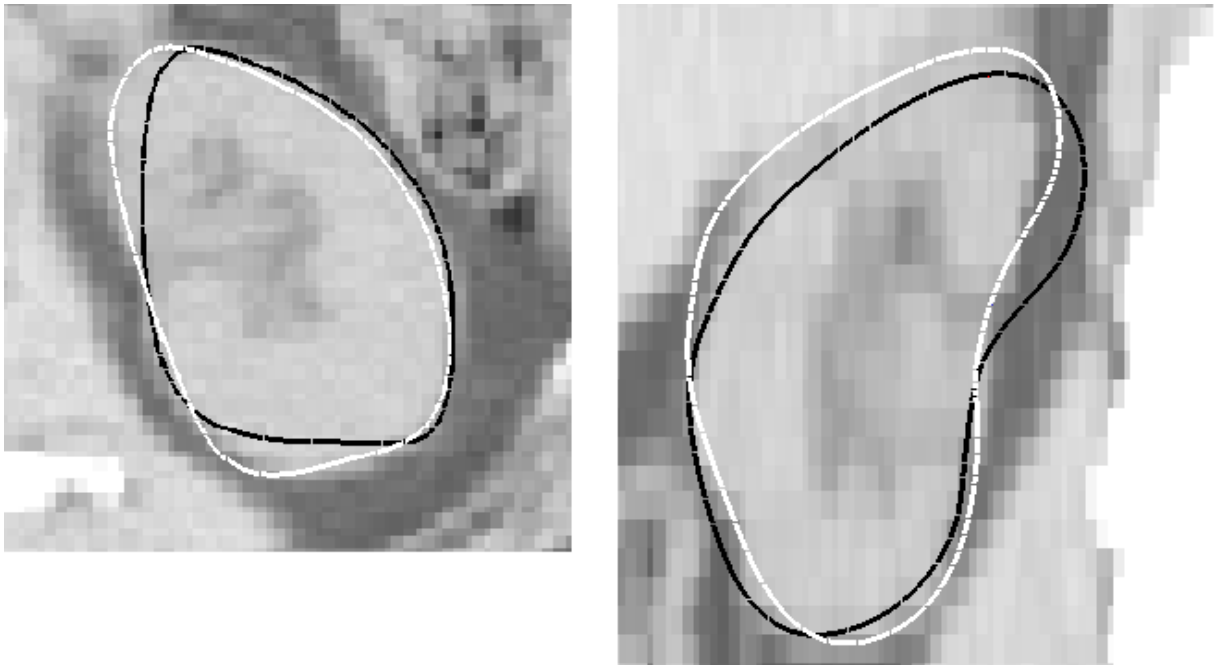

(a) (b)

Fig.3.18. Case 633R, Right Kidney - Initial Hand Placement (black contour), Final Segmentation (white contour) - (a) Axial Slice (b) Coronal Slice

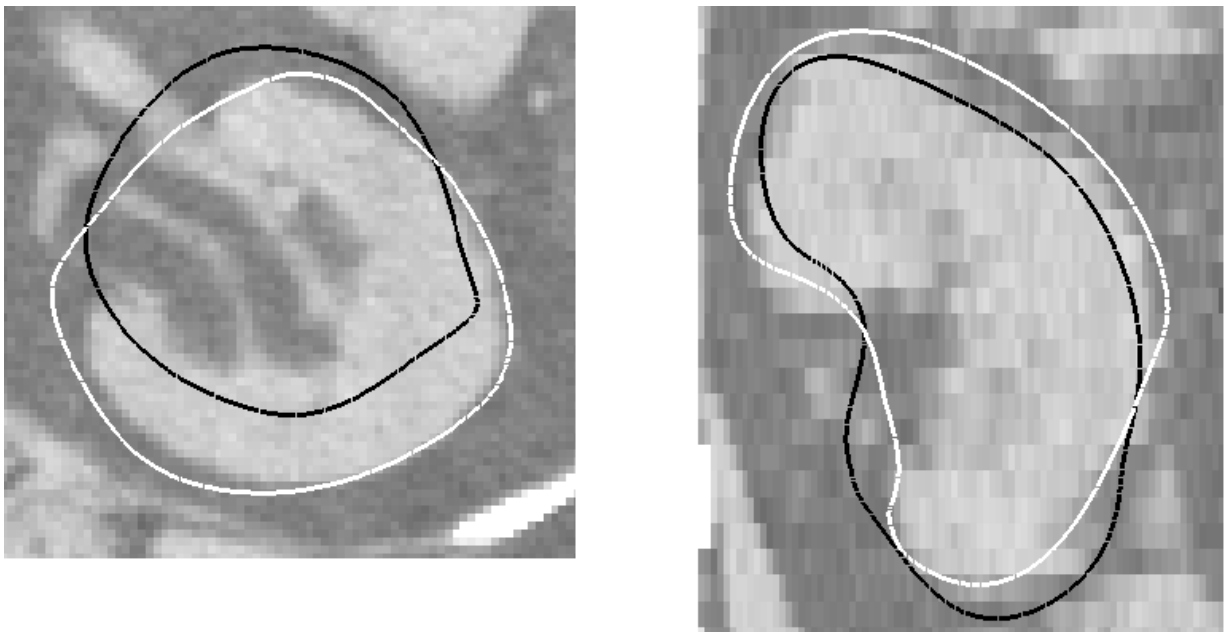

(a) (b)

Fig.3.19. Case 646L, Left Kidney - Initial Hand Placement (black contour), Final Segmentation (white contour) - (a) Axial Slice (b) Coronal Slice

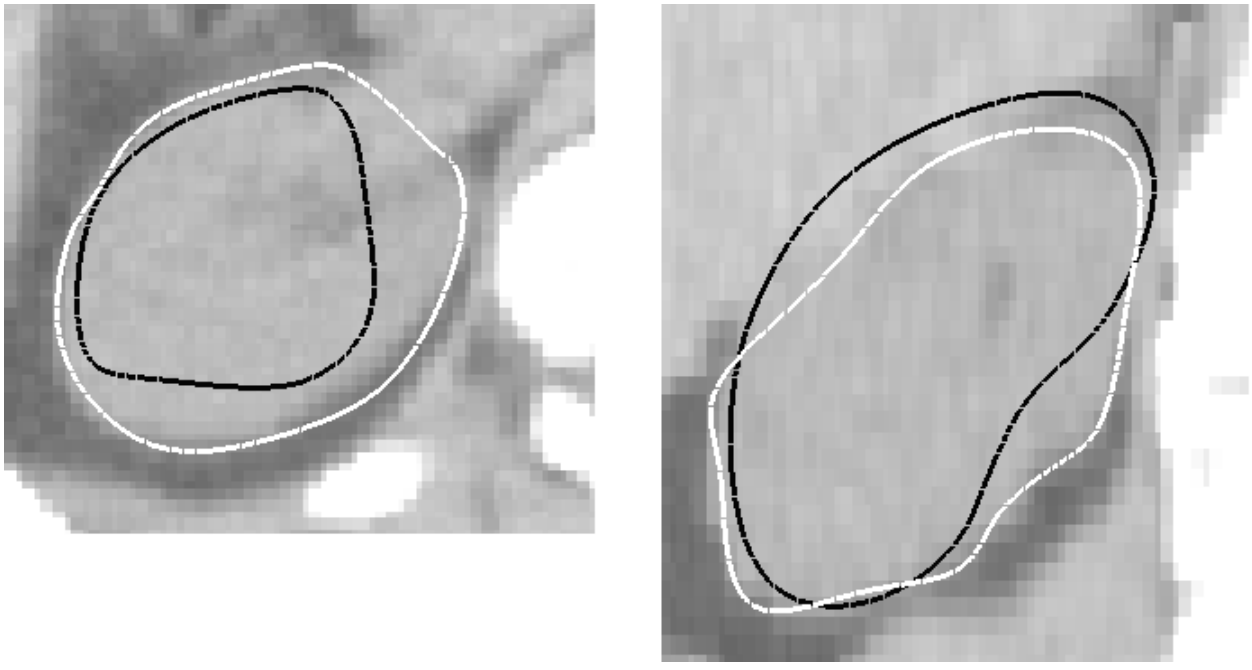

(a) (b)

Fig.3.20. Case 648R, Right Kidney - Initial Hand Placement (black contour), Final Segmentation (white contour) - (a) Axial Slice (b) Coronal Slice

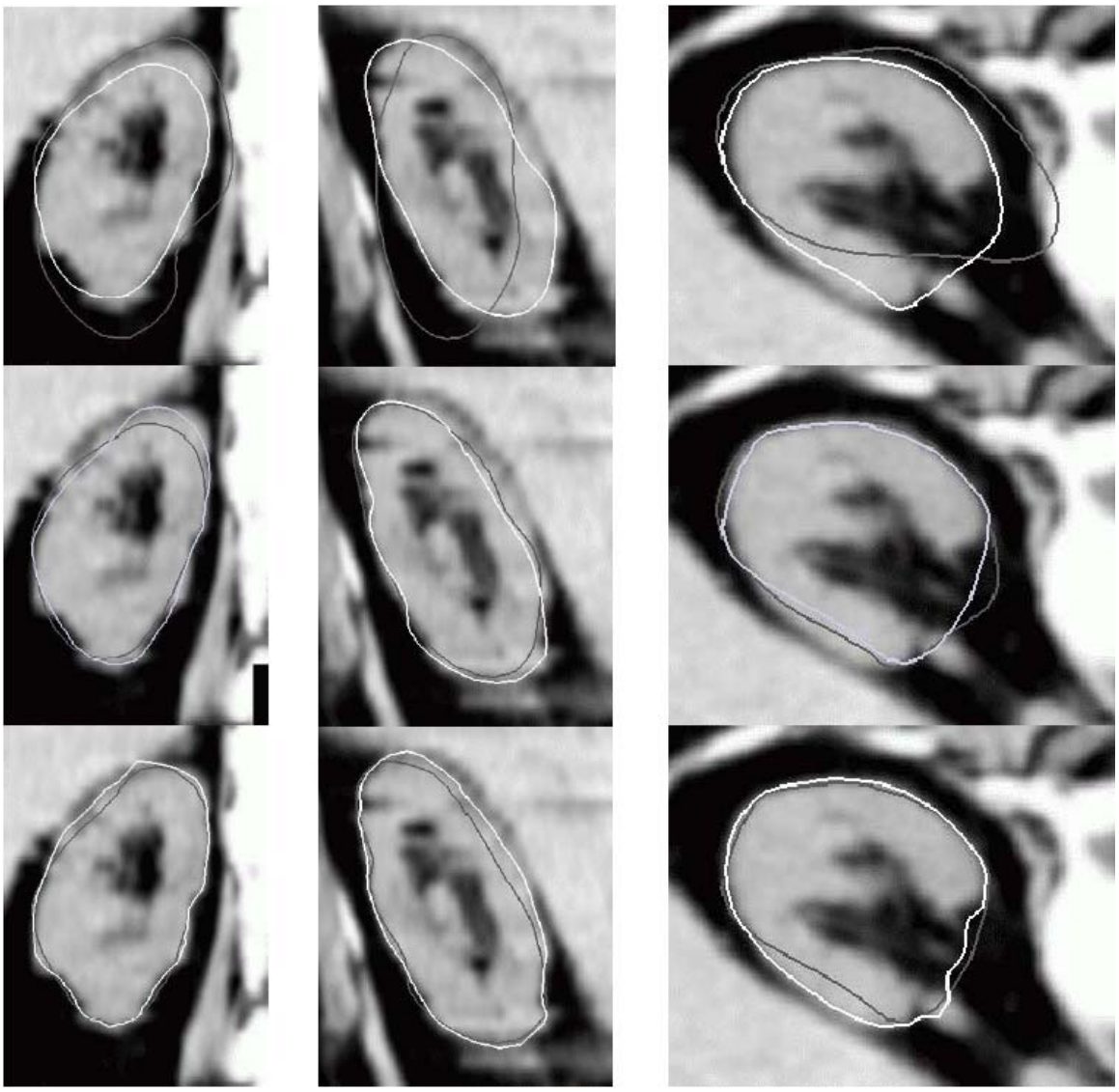

Fig.3.21. Segmentation, step-by-step: Initial Hand Placement (black contour), Final Segmentation (white contour)- all rows, from left to right, results on Coronal, Sagittal and Axial CT slices. The overlaid contours compare progress through two consecutive stages of deformation. **Top row**: The two stages are the initial position of the kidney model vs. the figural similarity transform and transform via PGA. **Middle**: Similarity transform + PGA vs. medial atom transformations. **Bottom**: medial atom transformations vs. 3D boundary displacements (This step was not used in the study). (Courtesy Pizer et al 2002)

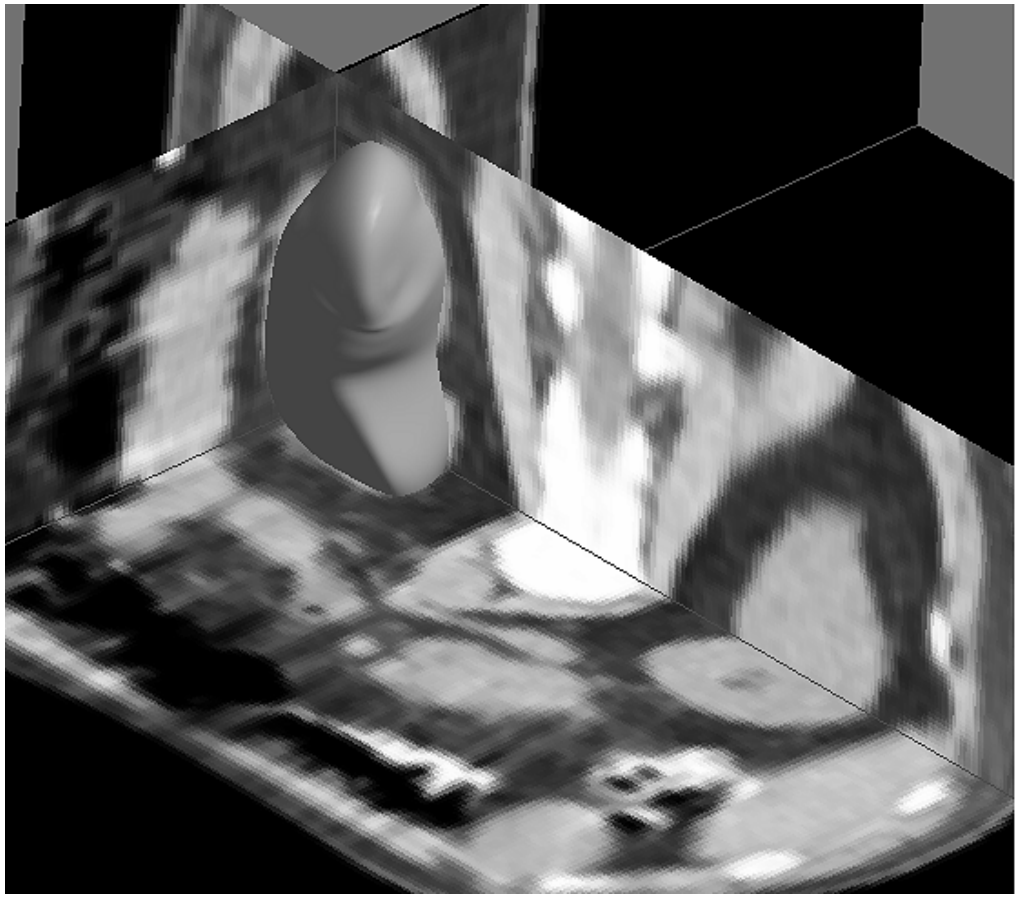

Fig.3.22. M-rep fit to a kidney in a CT image shown in axial planes.

3.5 Evaluation

The results obtained from the automatic segmentation method were compared to manual segmentation done by two different experts. The comparison between human and automatic segmentation was done using a software package, *Valmet* [Gerig 2001, Stough 2002], which involves voxel-based comparison using the following parameters:

(1) Volume overlap

An accepted measure of volume overlap is the intersection of the two volumes divided by their union. A score of 1 implies perfect agreement while 0 is complete disagreement. For the manual binary segmentations, a surface was computed using Marching Cubes [Lorensen and Cline 1987], with sub-voxel accuracy.

(2) *Maximum surface distance or Hausdorff distance*

This metric defines the largest distance between two surfaces. Given two contours A and B, for each point *a* on A, the minimal distance to all the points on contour B is calculated and the maximum of these distances is the 'worst case'. The Hausdorff metric is not symmetric since the closest distances from the first object

to the second (*a*) in Fig 3.16, are not the same as those from the second to the first (*b*) in Fig.3.16. This is accounted for by finally calculating,

$$Hauss\_Dist\ (A,B) = max\ \{\ dist\ (A,B),\ dist(B,A)\}$$

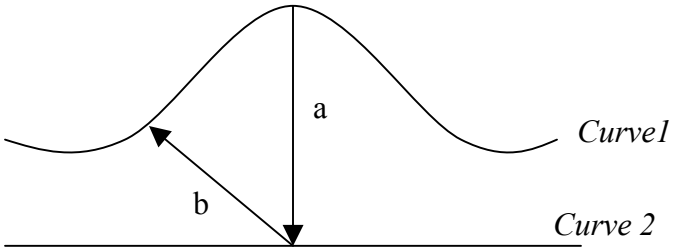

Fig. 3.23. The closest distance (a) from the first curve to the second is not the same as the closest distance (b) from the second curve to the first.

(3) *Mean surface distance*

The mean absolute surface distance describes how much on average the two surfaces differ. Point to point correspondence on the surfaces is required for this measure. The mean surface separation for a given kidney is defined in terms of closest points, i.e.,

$$\frac{1}{2}\left[\frac{1}{N_1}\left(\sum_{i=1}^{N_1} min_{j=1,\ldots,N_2}\left|\underline{y}_i^1 - \underline{y}_j^2\right|\right) + \frac{1}{N_2}\left(j\sum_{i=1}^{N_2} min_{i=1,\ldots,N_1}\left|\underline{y}_i^1 - \underline{y}_j^2\right|\right)\right]$$

where N_1 and N_2 are the respective numbers of boundary voxels in the two kidneys being compared, and $\underline{y}_i^1$ and $\underline{y}_j^2$ are the coordinates of the boundary voxel centers of the respective kidneys. This calculation is also not symmetric. A common average is therefore derived by combining the two averages.

CHAPTER 4- Results

This chapter summarizes the analysis of data generated using the locally varying intensity template for automatic segmentation. M-rep segmented kidneys were compared to manual segmentations performed by two human raters (A and B), using the metrics discussed in Chapter 3. The results of this comparison were weighed against an earlier study that used m-reps with a Gaussian derivative template based image match [Pizer et all 2002].

Manual segmentation by A and B was performed slice-by-slice using the program, MASK [Tracton 1994]. For the 12 target images, within-slice pixel size was approximately 1 mm, and slice thickness varied image to image between 3mm and 8 mm. Metrics in the following tables are given for 12 kidney pairs (12 right kidneys and corresponding left kidneys).

The results in Table 4.1 were obtained from an earlier study in which segmentation was performed using the Gaussian derivative based image match [Pizer et all 2002]. Metrics for m-reps segmentation compared to manual segmentation for the 24 kidneys are presented. Distances are in cm and volumes in cubic cm. Human raters

are A and B. C is the computer. The best and worst overlap cases are shaded gray. Mean and Standard Deviation values for each metric are also listed.

The results in Table 4.2 were obtained from segmentations performed using the locally varying intensity template generated from this study for image match. Metrics for m-reps segmentation compared to manual segmentation for the 24 kidneys are presented. Distances are in cm and volumes in cubic cm. Human raters are A and B. C is the computer. The best and worst overlap cases are shaded gray. Mean and Standard Deviation values for each metric are also listed.

Table 4.3 is a comparison between the volume overlaps obtained using the Gaussian derivative based template and the locally varying template for image match. The entries are volume overlap values expressed in percentage points. Negative values indicate that the volume overlap was greater for the Gaussian derivative based image match. The greatest and least differences are highlighted in gray for each rater.

Table.4.1. Results for Gaussian Derivative Template based Segmentations

Kidney code	Average surface distance (A to C)	Average surface distance (B to C)	Hausdorff distance (A to C)	Hausdorff distance (B to C)	Volume Overlap (A to C)	Volume Overlap (B to C)
630L	0.200	0.206	1.497	1.511	0.722	0.730
630R	0.249	0.221	0.829	1.059	0.723	0.733
633L	0.121	0.167	0.855	1.345	0.862	0.817
633R	0.157	0.210	1.050	1.233	0.830	0.790
634L	0.226	0.241	1.808	1.751	0.791	0.781
634R	0.258	0.221	1.706	1.657	0.735	0.779
635L	0.117	0.145	0.592	0.514	0.875	0.850
635R	0.156	0.200	0.852	1.130	0.837	0.802
636L	0.128	0.104	1.516	0.537	0.847	0.885
636R	0.148	0.154	1.249	1.168	0.835	0.837
637L	0.148	0.110	1.317	0.494	0.791	0.868
637R	0.168	0.162	0.799	0.787	0.805	0.810
638L	0.116	0.137	1.269	0.972	0.865	0.848
638R	0.305	0.327	1.685	1.678	0.756	0.744
639L	0.159	0.136	2.198	1.617	0.856	0.882
639R	0.089	0.077	1.234	0.897	0.917	0.919
640L	0.095	0.103	1.340	0.743	0.893	0.871
640R	0.123	0.155	1.456	1.203	0.872	0.853
642L	0.167	0.285	1.463	1.688	0.785	0.702
642R	0.145	0.200	0.689	0.785	0.829	0.795
646L	0.091	0.106	0.814	0.530	0.899	0.893
646R	0.126	0.157	1.248	1.329	0.857	0.840
648L	0.116	0.165	1.298	1.434	0.880	0.836
648R	0.129	0.190	1.335	0.973	0.835	0.794
Mean	**0.155**	**0.174**	**1.254**	**1.126**	**0.829**	**0.819**
SD	**0.055**	**0.059**	**0.391**	**0.408**	**0.055**	**0.056**

Table.4.2. Results for Locally Varying Template based Segmentations

Kidney code	Average surface Distance (A to C)	Average surface distance (B to C)	Hausdorff distance (A to C)	Hausdorff Distance (B to C)	Volume Overlap (A to C)	Volume Overlap (B to C)
630L	0.157	0.168	0.320	0.250	0.792	0.790
630R	0.213	0.178	0.490	0.310	0.753	0.768
633L	0.138	0.164	0.640	0.610	0.869	0.848
633R	0.132	0.144	0.650	0.40	0.878	0.868
634L	0.140	0.162	0.710	0.50	0.863	0.842
634R	0.245	0.260	0.550	0.370	0.662	0.681
635L	0.125	0.140	0.470	0.530	0.871	0.865
635R	0.146	0.178	0.530	0.550	0.850	0.836
636L	0.104	0.119	0.480	0.440	0.889	0.878
636R	0.148	0.138	0.610	0.480	0.849	0.864
637L	0.162	0.165	1.160	0.560	0.799	0.833
637R	0.156	0.160	0.590	0.550	0.842	0.840
638L	0.156	0.141	0.940	0.80	0.836	0.859
638R	0.127	0.114	0.870	0.690	0.849	0.871
639L	0.241	0.174	1.090	0.80	0.787	0.852
639R	0.228	0.160	0.880	0.780	0.816	0.869
640L	0.212	0.177	1.650	1.360	0.802	0.834
640R	0.182	0.137	0.690	0.510	0.847	0.884
642L	0.118	0.214	0.750	0.360	0.858	0.782
642R	0.157	0.232	0.540	0.620	0.827	0.772
646L	0.185	0.149	1.190	0.80	0.805	0.854
646R	0.194	0.111	0.80	0.410	0.797	0.857
648L	0.140	0.156	0.910	0.390	0.870	0.861
648R	0.187	0.146	0.70	0.410	0.825	0.863
Mean	**0.166**	**0.162**	**0.758**	**0.561**	**0.826**	**0.836**
SD	**0.039**	**0.034**	**0.294**	**0.232**	**0.048**	**0.046**

Table.4.3. Difference in Volume Overlap Values

Kidney Code	Difference in Volume Overlap (A to C)	Difference in Volume Overlap (B to C)
630L	0.069	0.059
630R	0.030	0.035
633L	0.006	0.031
633R	0.047	0.077
634L	0.071	0.061
634R	-0.074	-0.098
635L	-0.004	0.014
635R	0.012	0.033
636L	0.041	-0.008
636R	0.013	0.027
637L	0.007	-0.035
637R	0.037	0.029
638L	-0.029	0.010
638R	0.093	0.126
639L	-0.070	-0.031
639R	-0.101	-0.051
640L	-0.091	-0.038
640R	-0.026	0.030
642L	0.073	0.080
642R	-0.002	-0.023
646L	-0.095	-0.039
646R	-0.060	0.017
648L	-0.010	0.024
648R	-0.010	0.068
Mean	**-0.003**	**0.0165**
SD	**0.056**	**0.050**

Distribution of the Average surface distances for the 24 kidneys for rater A Vs m-rep for both Gaussian derivative as well as the template based segmentation.

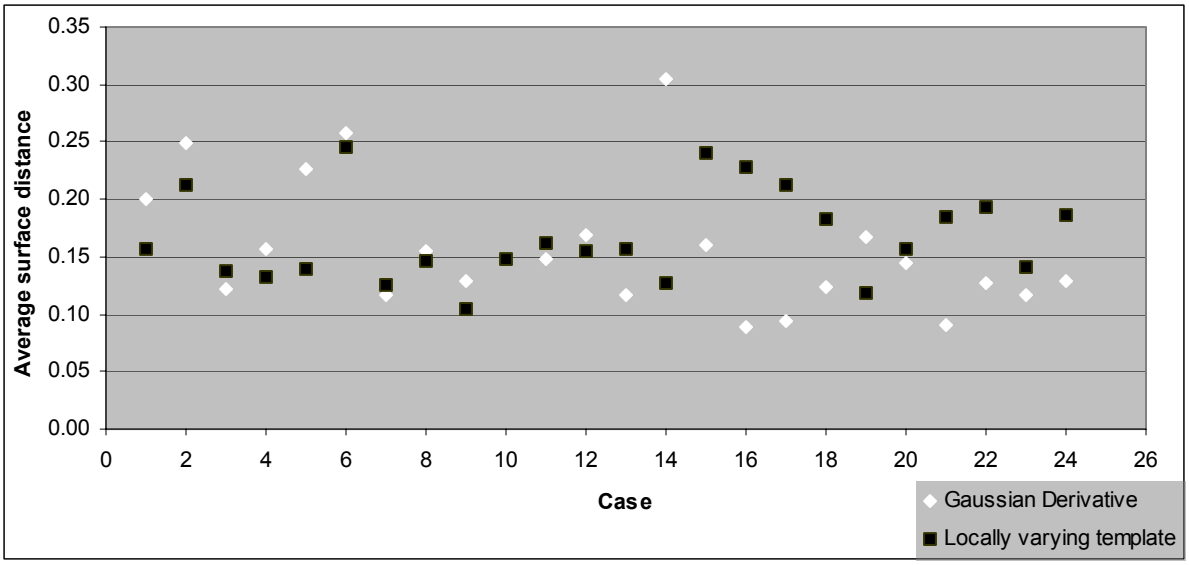

Fig.4.1. Average surface distance distribution for A Vs C

Distribution of the Average surface distances for the 24 kidneys for rater B Vs m-rep for both Gaussian derivative as well as the template based segmentation.

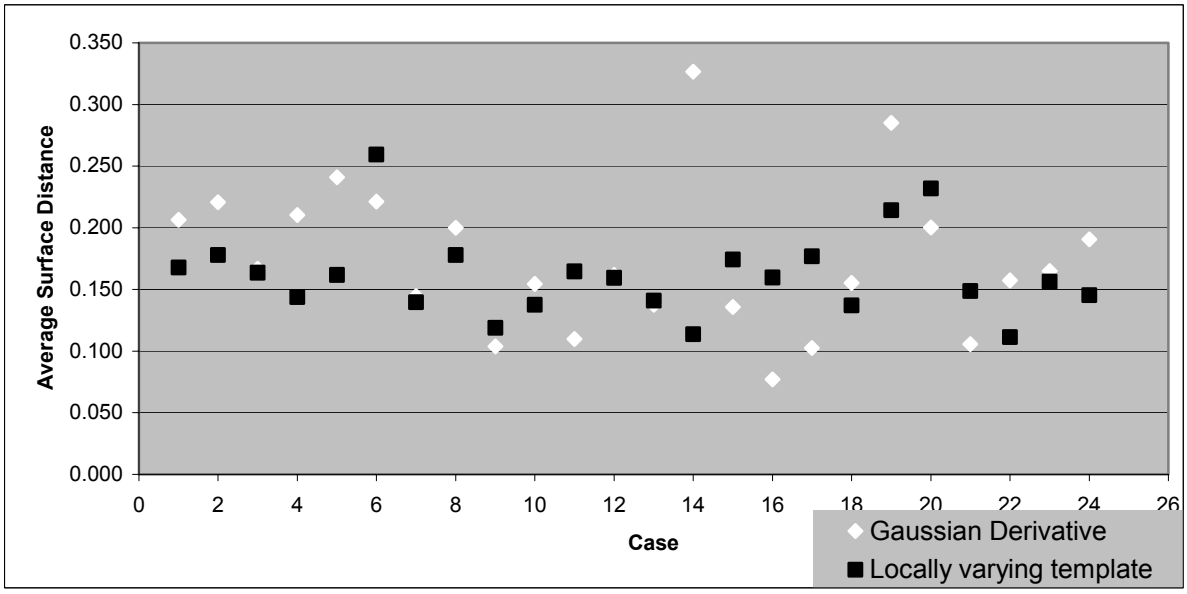

Fig.4.2. Average surface distance distribution for B Vs C

The results from Tables 4.1, 4.2, 4.3 and Figures.4.1 and 4.2, show that out of the 24 kidneys segmented by rater A, the segmentation done using the locally varying template method generated better results for 12 of the cases. On the other hand, out of the 24 kidneys segmented by rater B, the template method generated better results for 19 of the cases. The average increase in volume overlap over all the cases was 1.3%. The mean surface separation between human segmentations and M-rep segmentation, averaged over all the cases was 0.33cm for segmentation done using the Gaussian derivative template while it was 0.32cm for segmentation done using the locally varying template.

4.1 Comparison of Segmentation Results

The following figures illustrate cases in which the results in the segmentation using the locally varying intensity template (white contours) showed improvement over segmentation results obtained using the Gaussian derivative template (black contours) for image match.

The volume overlap for Case 634L (from Table.4.1) was 79.1% (A to C) and 78.1% (B to C) for segmentation done using the Gaussian derivative template, while (from Table.4.2) it was 86.3% (A to C) and 84.2% (B to C) for segmentation done using the locally varying intensity template for image match. Visual inspection indicated that the contrast at the boundary between the spleen and the left kidney was very

poor in this particular case and the spleen also appeared brighter in some areas along this boundary (Fig.4.3).

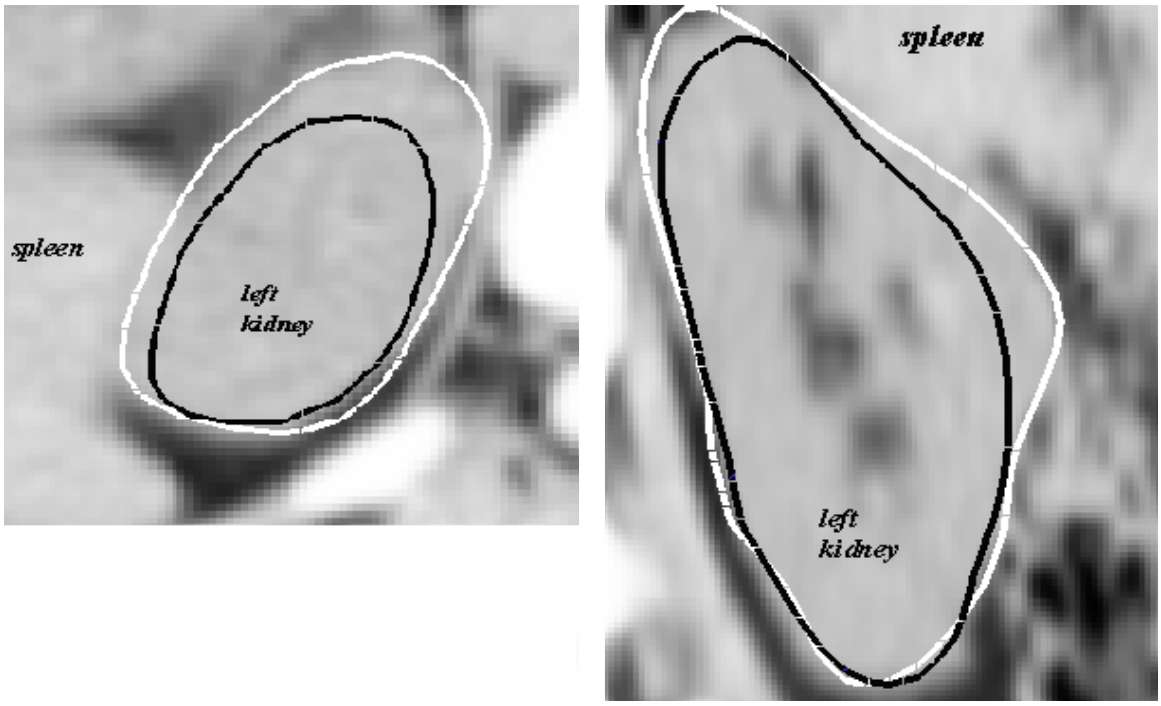

(a) (b)

Fig.4.3. Case 634L - Gaussian Derivative (black contour) and Locally Varying Template (white contour) based segmentations - Left Kidney (a) Axial View (b) Coronal View

The distribution of the three different filter types along the surface of the left kidney for the locally varying template based approach shown in Fig.3.14 indicates both the dark-to-light and notch filters in this region which agrees with the image data in this example. On the other hand, the Gaussian derivative based segmentation was unable to find the exact kidney boundary due to low image match in this particular kidney-spleen boundary region.

The volume overlap for Case 630R (from Table.4.1) was 72.3% (A to C) and 73.3% (B to C) for segmentation done using the Gaussian derivative template, while (from Table.4.2) it was 75.3% (A to C) and 76.8% (B to C) for segmentation done using the locally varying intensity template for image match. Visual inspection indicated that the high contrast at the liver-kidney boundary due to brighter intensities in the liver caused a repulsive force when the Gaussian derivative template was used for image match (Fig.4.4).

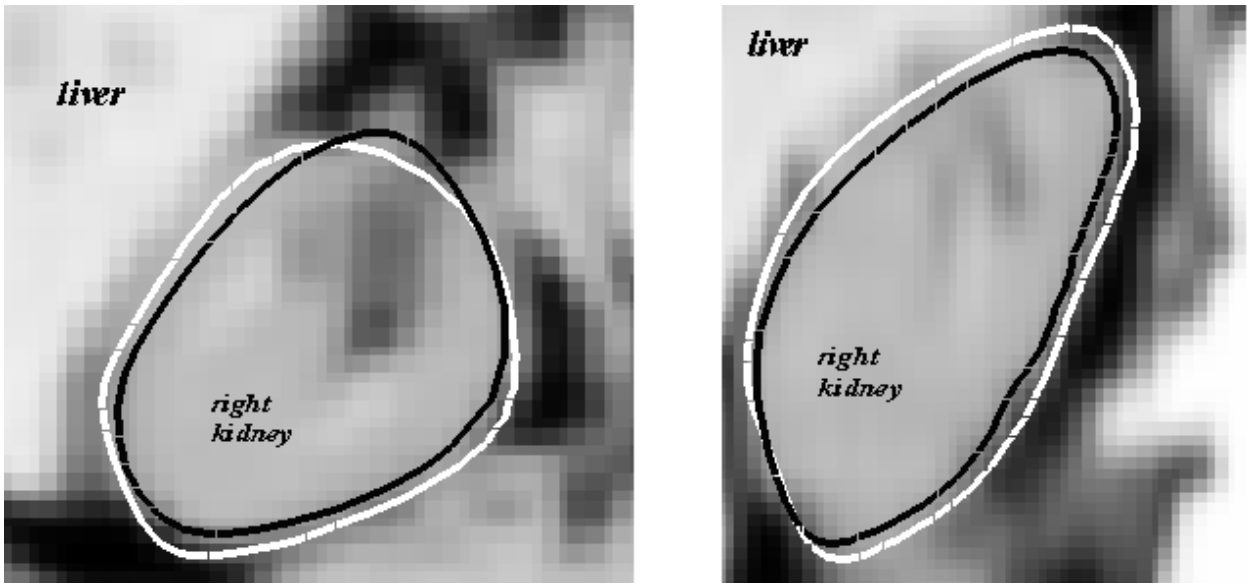

(a) (b)

Fig.4.4. Case 630R - Gaussian Derivative (black contour) and Locally Varying Template (white contour) based segmentations - Right Kidney (a) Axial View (b) Coronal View

The distribution of the three different filter types along the surface of the right kidney for the locally varying template based approach shown in Fig.3.13 indicates the dark-to-light filter in this region which agrees with the image data and resulted in a better image match as compared to the Gaussian derivative.

The following figure (Fig.4.5) illustrates a case in which the result when the Gaussian derivative template (black contour) was used for image match was better than segmentation result from the locally varying template (white contour). The volume overlap for Case 634R (from Table.4.1) was 73.5% (A to C) and 77.9% (B to C) for segmentation done using the Gaussian derivative while (From Table.4.2) it was 66.2% (A to C) and 68.1% (B to C) for segmentation done using the locally varying intensity template for image match.

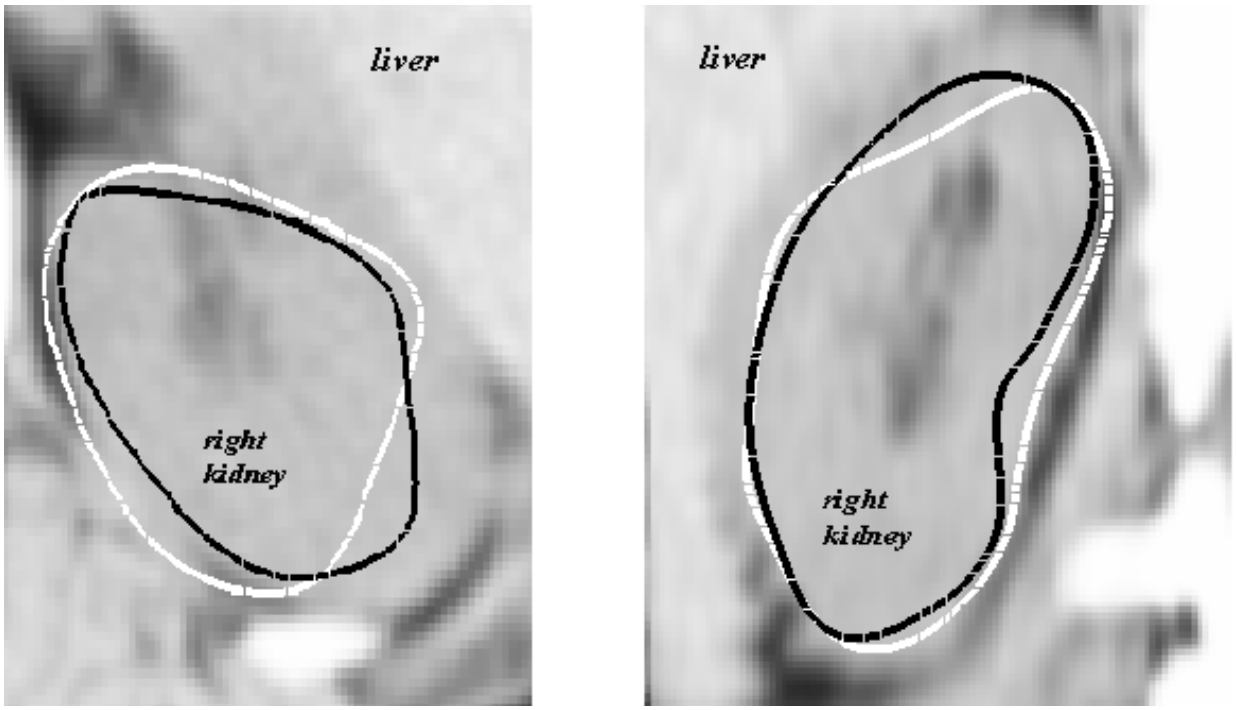

(a) (b)

Fig.4.5. Case 634R - Gaussian Derivative (black contour) and Locally Varying Template (white contour) based segmentations - (a) Axial View (b) Coronal View

A significant finding from this particular case was the fact that there was a certain amount of human intervention in the segmentation results produced from the earlier

study which used the Gaussian derivative template for image match. The similarity transform stage where the model is deformed as a whole (discussed in Chapter 2) was eliminated in this case during segmentation and the hand initialization was directly used as input to the atom deformation stage. On the other hand, segmentation in the present study was performed with no such human intervention to generate better segmentations but the results were comparable. To make a better comparison between the two segmentation results for this case, the similar procedure (eliminating model stage) was carried out for segmentation using the locally varying template for image match (Fig.4.6), by human intervention and the metrics of comparison (discussed in Chapter 3 and Tables 4.1 and 4.2) were recalculated. The volume overlap values were 80.8% (A to C) and 77.9% (B to C). This shows a significant improvement from the values in Table.4.2 for this case when there was no human intervention involved. It is possible to attribute this change in segmentation at the model stage to the fact that the geometry of the object might not have been completely defined by the PGA modes used for this study at the end of the first step in the segmentation process (Chapter 2, Section 2.2). This possibly caused the image match to be calculated on a local optimum based on the width of the collar region (discussed in Chapter 2). Further investigation is required to arrive at firm conclusions for this particular case.

Another interesting observation during the study was a particular case (638R), which revealed that segmentation done using the locally varying template was closer to segmentation done by a human expert. This CT image had significant breathing

artifacts that created spurious sections that were not included in the segmentations by both the raters (Fig.4.7 and Fig.4.8). The earlier study performed with m-reps using the Gaussian derivative for image match, resulted in a segmentation that included this portion of the kidney (Fig.4.9).

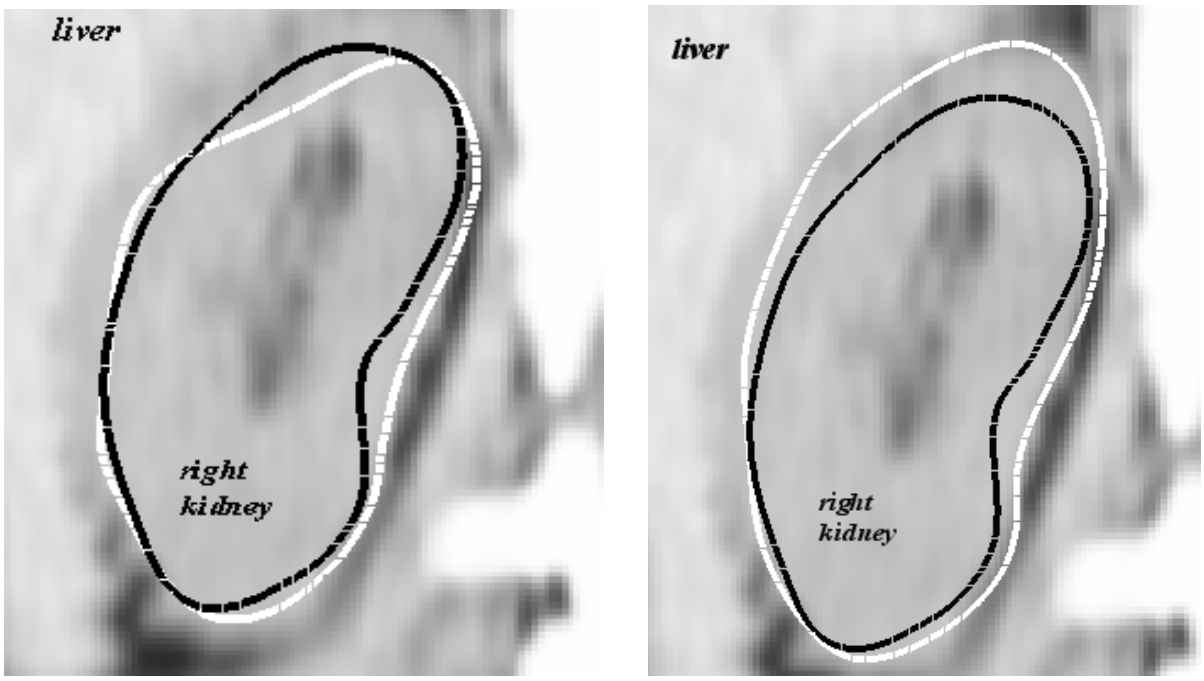

(a) (b)

Fig.4.6. Segmentation results without and with human intervention for the locally varying template method. Case 634R - (a) Gaussian Derivative (black contour) based segmentation with human intervention and Locally Varying Template (white contour) based segmentation without human intervention (b) Gaussian Derivative (black contour) based segmentation with human intervention and Locally Varying Template (white contour) based segmentation also with human intevention

On the other hand, segmentation via m-reps on the same image with the locally varying template for image match, produced a model which did not include this section of the kidney (Fig.4.9) and thus had a better volume overlap when compared

to the manual segmentations. Since the image data was ambiguous due to the motion artifacts, no firm conclusion could be drawn. However, auto segmentation could find either of the two possible results.

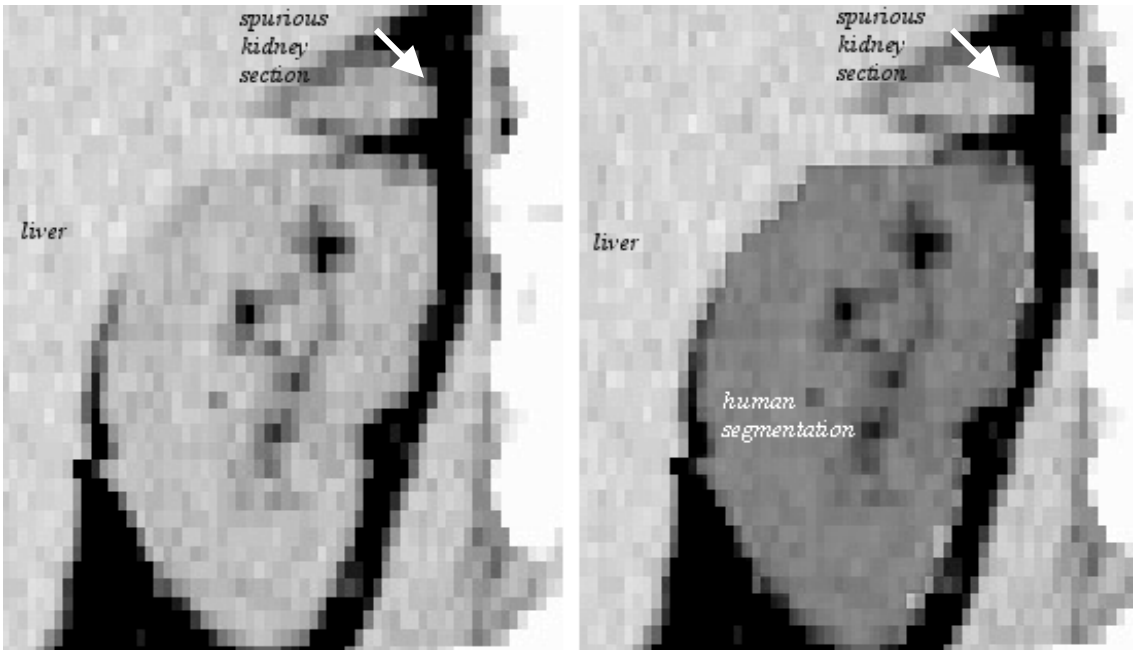

(a) (b)

Fig.4.7. Case 638R (a) Coronal view of image with a spurious kidney section due to motion artifact (b) Human segmentation of the same kidney shaded in a darker gray.

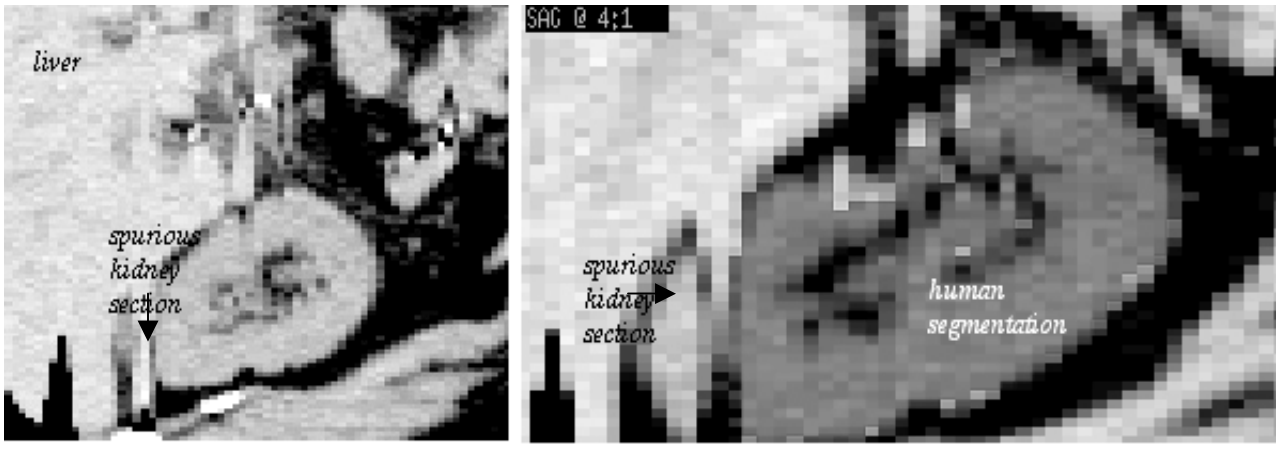

(a) (b)

Fig.4.8. Case 638R (a) Sagittal view of image (b) Human segmentation shaded in a darker gray

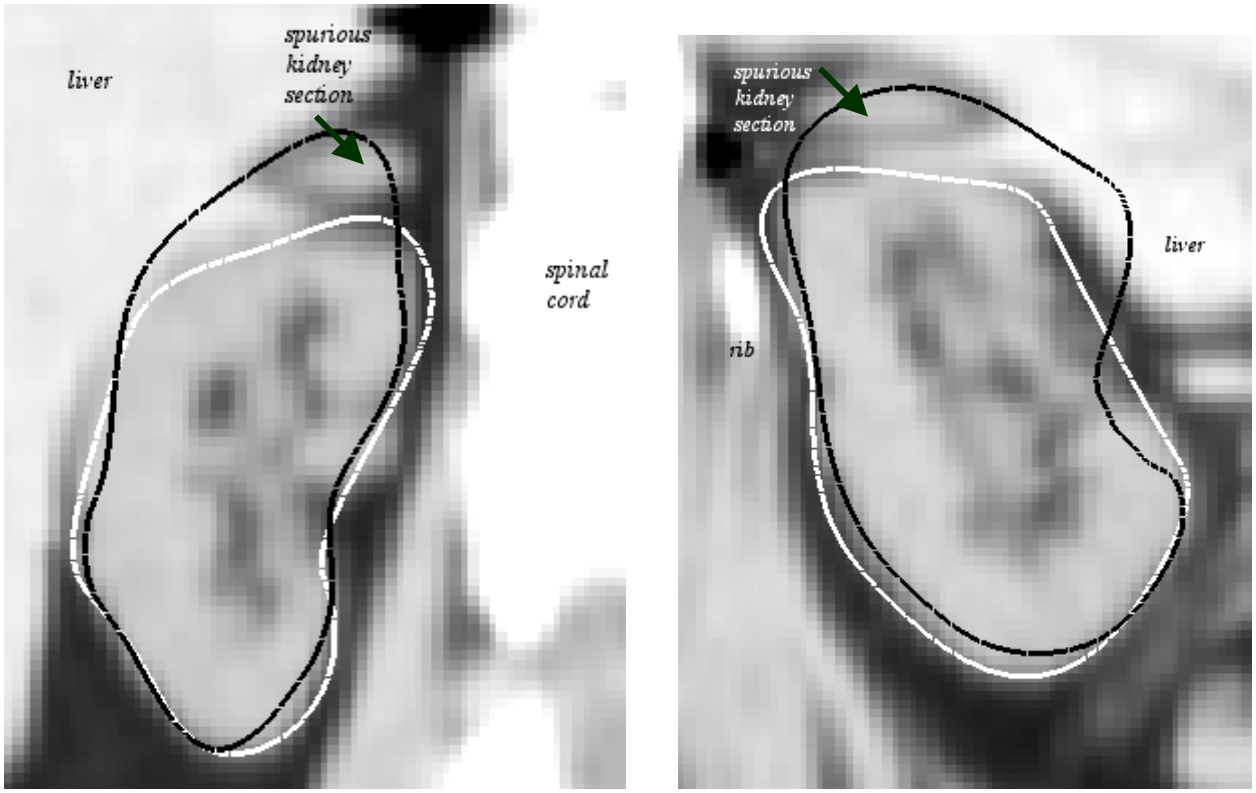

Fig.4.9. Case 638R (right kidney) - Shows a spurious section (Coronal and Sagittal slices) produced due to motion artifact. The black contour was segmentation done with Gaussian derivative image match and the white contour is segmentation done using the locally varying template for image match.

A test was also conducted as part of this study to eliminate any bias in the final segmentation due to differences in the initial hand-placement of the M-rep model. Two cases were selected and the first step in the deformation process was performed with ten different interactive hand-placements for each of the cases. The displacements were selected to approximately position the kidney m-rep in a suitable position in the image before the first step in the m-rep segmentation process. The differences in the placements varied to a maximum of 0.015mm (tenth of a voxel in the image) in X. The similarity transform (geometric penalty term) was calculated at the end of the first step and saved for each of the trials. These

numbers were compared to eliminate any possibility of bias due to variation in hand-placements by the user and are listed in Table.4.4.

The numbers from Table.4.4 and Fig.4.10 indicate that there is a slight variation (maximum of 8.7% for a placement difference of 0.015mm) at the end of the first step due to differences in the hand-placements before initializing m-rep segmentation. This indicates that the bias introduced due to initial hand-placements did not severely influence the m-rep segmentations.

Table.4.4. Image Match Values for 10 Trials

	Image Correlation	
Case	**639R**	**646R**
Trial 1	0.674	0.602
Trial 2	0.690	0.608
Trial 3	0.687	0.586
Trial 4	0.686	0.608
Trial 5	0.677	0.615
Trial 6	0.669	0.618
Trial 7	0.684	0.640
Trial 8	0.668	0.631
Trial 9	0.685	0.616
Trial 10	0.667	0.584
Mean	**0.687**	**0.611**
SD	**0.008**	**0.017**

Table.4.4. Image match values for 10 trials for two separate cases (least and most variation). Geometry to image match term is measured in rms-proportional intensity squared units

resulting from the correlation of the template image and the target image, normalized by local variability in these image intensities [Pizer et al 2001].

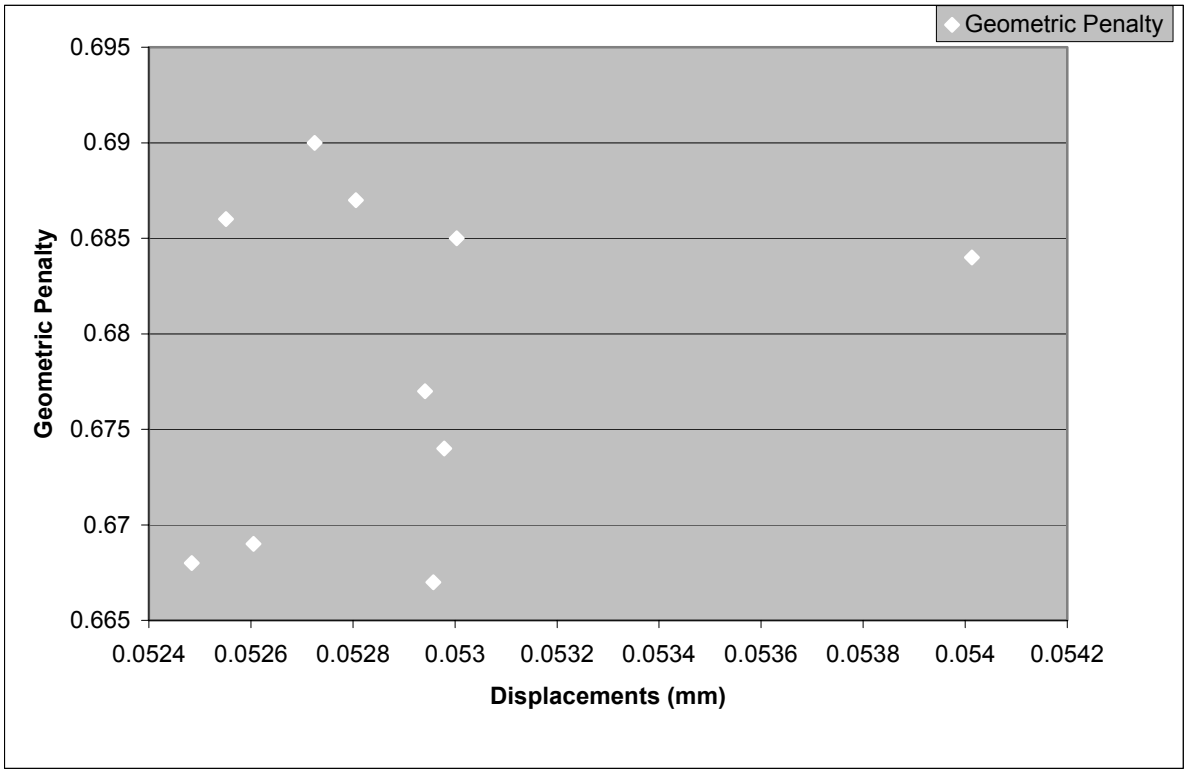

Fig.4.10. Distribution of values for the Similarity Transform (represented by Geometric Penalty) at the end of the first step in the m-rep segmentation process for 10 different hand-placements for the same image (639R). The displacements are in mm along the X-direction in the image.

CHAPTER 5 - Conclusions and Discussion

5.1 Analysis of the Results

The main idea of this study was to analyze a medical image segmentation method that uses deformable medial models known as m-reps. This work describes a way of obtaining a locally varying template based on intensity profiles measured at many points over the surface of a given object in 3D.

The results of this study show that given set of training images, a common intensity template can be generated, which in the majority of cases studied in the investigation, provided a slightly better image match to the target image data as compared to segmentation done using the Gaussian derivative template.

The Gaussian derivative template was designed such that there is increased response at target object boundaries surrounded by regions with darker intensities. There are several disadvantages in using this kind of analytic template. For example, a kidney m-rep can penetrate bony objects such as ribs or vertebral bodies because the high dark-to-light contrast results in a high model to image match value when a section of the m-rep boundary overlays a brighter structure (Fig.5.2). Similarly, the boundary at the liver does not provide a strong image match for the m-

rep when the Gaussian derivative is used since the liver usually has brighter or equal intensity as compared to the kidney in most CT images (Fig.5.1).

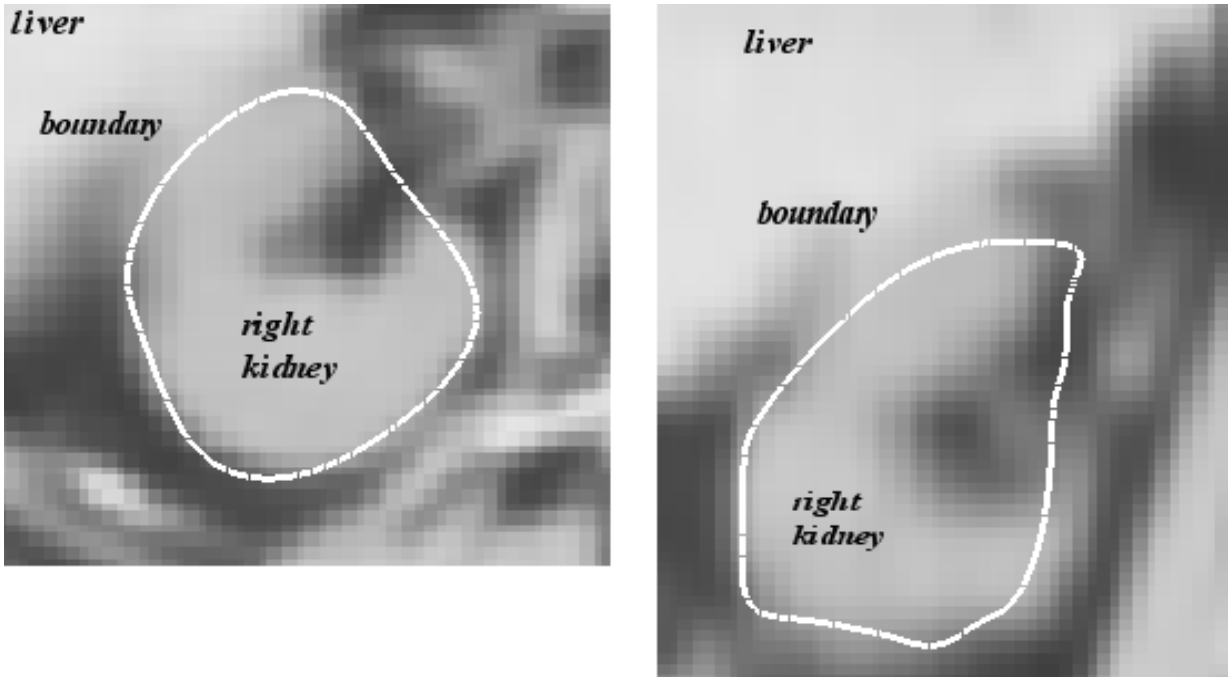

Fig.5.1. Example illustrating poor contrast at the kidney-liver boundary

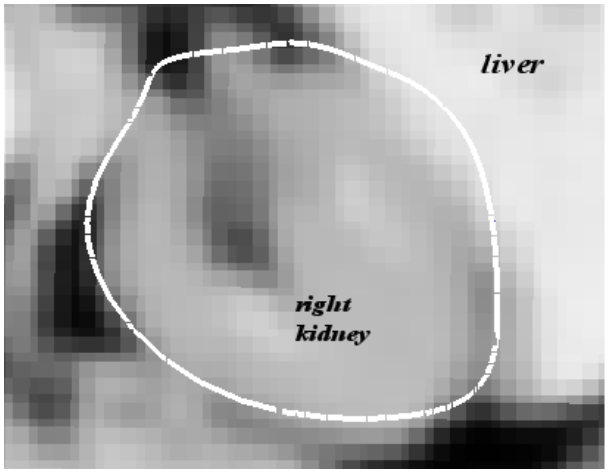

Fig.5.2. Example illustrating slight penetration of m-rep into the liver at the end of the first step during segmentation when Gaussian derivative is used for image match

M-rep segmentation using a locally varying intensity template provided improvement in image match since the template was generated on a population of training images which better represents intensity variation in an image. On the other hand, the Gaussian derivative uses a fixed intensity value over the entire boundary which is unsuitable to extract objects that appear without high contrast over most of their boundary. This finding supports the notion that more sophisticated intensity templates that use an arbitrarily large number of intensity profiles (not just three), can do an even better job.

An important observation of this investigation was the degree of automation that the locally varying intensity based method achieved. The m-rep segmentations from the previous study involved a certain amount of user-intervention to achieve accurate segmentations in some of the cases as discussed in Chapter 4 (Case 634R - Fig.4.6). Case 635R was another such example. The similarity transform step of the m-rep segmentation process was eliminated and the hand-placement of the model was directly used for atom deformation for this case in the earlier study. The shape of the kidney in this particular case was more elongated as compared to the kidneys in the other images (Fig.5.3). The similarity transform failed to capture the entire shape description of the kidney, for two main reasons. Firstly, this transformation did not involve PGA along with the similarity transform and more importantly the boundary seemed to be repelled by both the liver on one side and the spinal cord on the other when the Gaussian derivative template was used for image match.

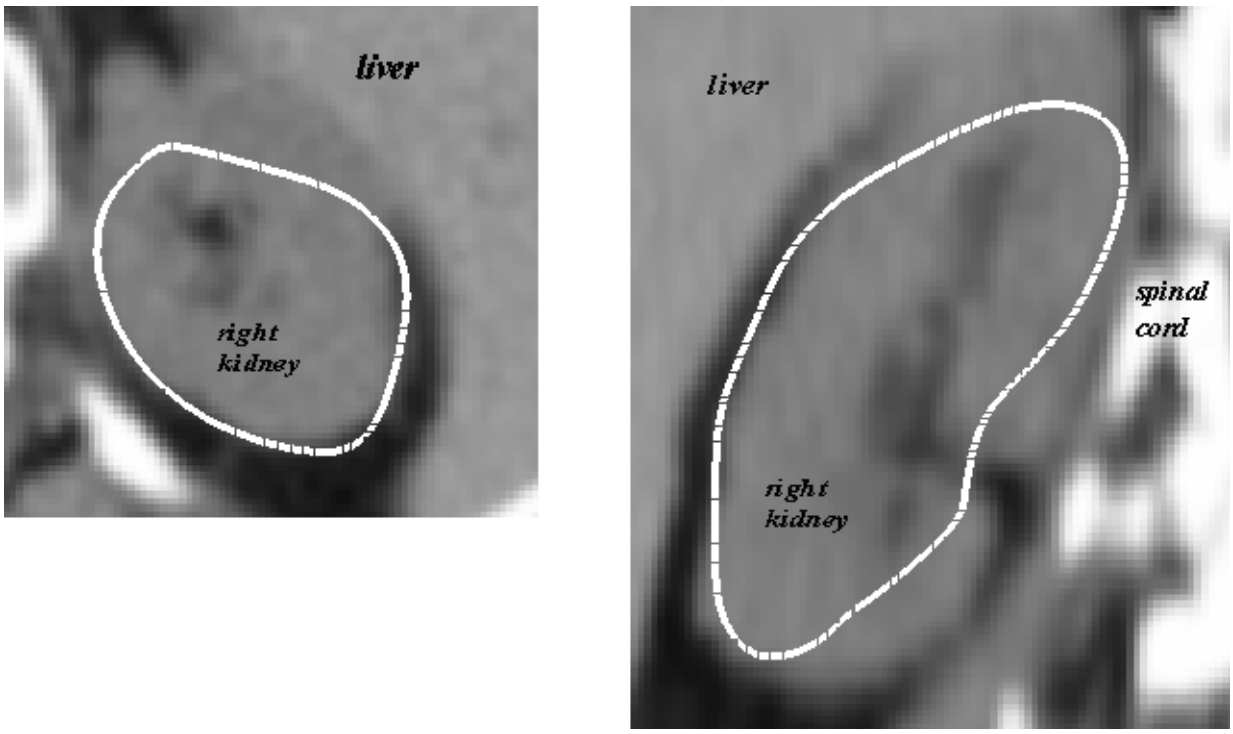

(a) (b)

Fig.5.3. Case 635R (a) Axial View (b) Coronal View. Contours of m-rep boundary at the end of the similarity transform stage with image match calculated using the Gaussian Derivative Template.

A similar example was Case 642R. The parameter that controls the variation of an atom with respect to its neighbors (as described in Chapter 2) was relaxed in the atom deformation stage during segmentation of this particular image to better capture the shape of the kidney. This was possibly again a result of the fact that the model deformation (Fig.2.5) prior to the atom deformation stage did not capture enough geometry information due to surrounding brighter intensities of the liver and spinal cord which cause decrease in image match values when the Gaussian image match is measured.

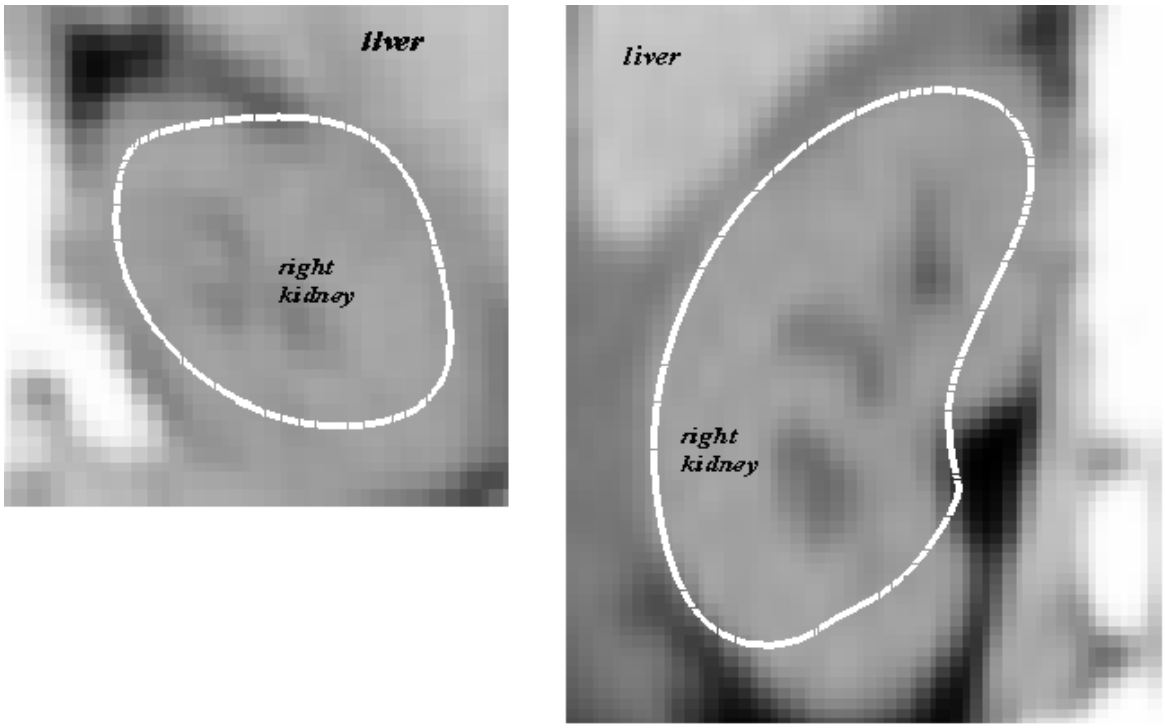

(a) (b)

Fig.5.4. Case 642R (a) Axial View (b) Coronal View. Contours of m-rep boundary at the end of the similarity transform stage with image match calculated using the Gaussian Derivative Template.

These two cases (Fig.5.3 and Fig.5.4) and case 634R (Chapter 4, Fig.4.6) indicate the fact that there were certain changes made by human intervention to match segmentations to specific target images in the previous study. Human intervention in these cases improved the quality of segmentation. The present study which used the locally varying template based approach for image match, was conducted with constant parameters over all the cases (for both the similarity transform with PGA as well as the atom deformation stages), which resulted in segmentations comparable, if not better, to the segmentations from the previous study. This indicates an improvement in the amount of automation involved during segmentation when

profiles generated from a population of images are used to measure the match of the model to the image rather than a single analytical profile over the entire surface of an m-rep model.

The results from the study showed improvement in the segmentations for 65% of the entire set of kidneys segmented. One of the limitations in the present study was the pre-selection of the target data set, which was chosen as the target set for the earlier study based on certain selection criteria that favored the Gaussian derivative template for image match. These were CT images which had relatively high-contrast boundaries along the kidneys. On the other hand, the training data set that was selected to generate the locally varying intensity template did not have high contrast along the boundary of the kidney in most of the images. The manual segmentations initially generated were also dependent on intensity windowing of the images. This is possibly another limitation of the method, since there can be a huge amount of inter-operator variability in human segmentations depending on the intensity window selected and only segmentations from a single human rater were considered in generating the template. The primary metric used for comparison was volume overlap. Use of other more precise metrics might probably better illustrate the variations in the results. Segmentation in this study also did not involve the final step of the m-rep segmentation process, namely, fine-scale boundary refinement.

5.2 Future Directions

The study of the current technique was one of the preliminary studies conducted using a locally varying intensity template for segmentation using m-reps. A more extensive analysis of this technique would be to compare results using a template generated for more than three filter types, since profile information along normals drawn at boundary points cannot be optimally represented with just three filters. A complete answer to the question of how to classify intensity profiles, could be produced based on statistical studies of the variation of each of the profiles along the boundary normals for all the training cases under consideration and analysis of Eigen modes and Principal Components of the entire data set. Taking a much larger data set into consideration would perhaps produce more statistically significant results.

Another interesting future direction in the training process would be the study of a template generated not based on profiles along normals at individual boundary points, but on profiles at each boundary point generated by taking the profiles along normals of neighboring boundary points into consideration as well. In other words, the response at a particular point would be the 'weighted' sum of responses of all neighboring profiles. The training images in this study were blurred to remove high frequency noise, but the possibility of residual noise even after blurring cannot be eliminated. A training process involving responses dependent on neighboring profiles would provide a robust method of handling noise in the training image data since considering the responses of neighbors to calculate the profile at a particular

point would eliminate the possibility of assigning an inappropriate filter due to noise at that point.

The present study was performed using a 5X3 mesh kidney m-rep (5 rows and 3 columns). A significant area of study would be the use of an m-rep model with higher density (more number of rows and columns describing the same shape) for profile-based segmentation. A sample test conducted during this study resulted in a profile distribution for a 6X4 kidney m-rep model that was different from the profile distribution obtained for the 5X3 model. This is possibly due to differences in curvature and the variation in the fit of the model to the image data. A model with higher density would also provide a means of smoothing the m-rep model rather than smoothing the image data prior to segmentation.

References

1. James Z Chen, Gregg Tracton, Manjari Rao, Sarang Joshi, E.L Chaney, Stephan M.Pizer. Comparison of Automatic and Human Segmentation of Kidneys from CT Images. *American Society for Therapeutic Radiation Oncology*, October 2002.

2. T. F. Cootes and C. J. Taylor. Statistical models of appearance for medical image analysis and computer vision. *Proc. SPIE Medical Imaging*, 2001.

3. Jessica R. Crouch, Stephen M. Pizer, Edward L. Chaney, Marco Zaider. Medially Based Meshing with Finite Element Analysis of Prostate Deformation. *Information Processing in Medical Imaging,* 2003.

4. P.Thomas Fletcher, Conglin Lu, Sarang Joshi. Statistics of Shape via Prinicpal Component Analysis on Lie Groups. *Computer Vision and Pattern Recognition*, June 2003.

5. Stefan Grobkopf. Volume Visualization for Improved Radiation Treatment Planning in Oncology. *Computer Graphik Topics special edition 73-47*Stephen

6. Yongwon Jeong (RPI), Dr.Richard J.Radke (RPI), Dr.Badri Roysam (RPI), Dr.Daniel Freedman (RPI), Dr.George TY Chen (MGH), Philip Yoon (RPI). Automatic segmentation of the prostate and surrounding structures for image-guided radiotherapy.

7. Sarang Joshi, Stephen Pizer, P. Thomas Fletcher, Andrew Thall, and Gregg Tracton. Multi-scale 3D Deformable Model Segmentation Based on Medial Description. *Information Processing in Medical Imaging*, June 2001. 2082: 64-77 & IEEE TMI 21(5): 538-550.

8. Maria Petrou, Panagiota Bosdogianni. Image Processing -The Fundamentals. *John Wiley & sons Ltd*. 1999.

9. M. Pizer, James Z. Chen, P. Thomas Fletcher, Yonatan Fridman, Daniel S. Fritsch, A. Graham Gash, John M. Glotzer, Michael R. Jiroutek, Sarang Joshi, Conglin Lu, Keith E. Muller, Andrew Thall, Gregg Tracton, Paul Yushkevich, Edward L. Chaney. Deformable M-Reps for 3D Medical

Image Segmentation. *International Journal of Computer Vision,* September 2002.

10. Stephen M. Pizer, Guido Gerig, Sarang Joshi, Stephen R. Aylward. Multiscale Medial Shape-Based Analysis of Image Objects. To appear in *Proceedings of the IEEE 2003.*

11. Stephen M. Pizer, Sarang Joshi, P. Thomas Fletcher, Martin Styner, Gregg Tracton, James Z. Chen. Segmentation of Single-Figure Objects by Deformable M-reps. *Medical Image Computing and Computer-Assisted Intervention*, October 2001. Lecture Notes in Computer Science, Volume 2208: 862-871.

12. Stephen M. Pizer, P. Thomas Fletcher, Andrew Thall, Martin Styner, Guido Gerig, Sarang Joshi. Object Models in Multiscale Intrinsic Coordinates via M-reps. *Generative Model Based Vision*, June 2002.

13. Stephan M. Pizer, Daniel S. Fritsch, Paul A. Yushkevich, Valen E. Johnson, Edward L. Chaney. Segmentation, Registration, and Measurement of Shape Variation via Object Shape. *IEEE/ Trans. Med. Imaging*, October 1999, 18(10): 851-865.

14. John C Russ. The Image Processing Handbook. *CRC Press Inc. 2nd Edition*, 1995.

15. Jefferey Shufelt. Geometric Constraints for Object Detection and Delineation. *Kluwer Academic Publishers,* 2000.

16. Milan Sonka, Vaclav Hlavac, Roger Boyle. Image Processing, Analysis and Machine Visison. *Brooks/Cole Publishing Company 2nd Edition,* 1999.

17. L. Staib and J. Duncan. Model-based deformable surface finding for medical Images. *IEEE Trans. on Medical Imaging*, Vol.15, No.5, pp.720-731, October 1996.

18. .Martin Styner, Guido Gerig. Medial models incorporating object variability for 3D shape analysis. *Information Processing in Medical Imaging*, June 2001.

19. Andrew Thall. Fast C^2 Interpolating Subdivision Surfaces using Iterative Inversion of Stationary Subdivision Rules. *Technical Report TR02-001*, Feb 2003.